

An Adaptive-Rank Approach with Greedy Sampling for Multi-Scale BGK Equations

William A. Sands^{*1}, Jing-Mei Qiu^{†1}, Daniel Hayes^{‡1}, and Nanyi Zheng^{§1}

¹Department of Mathematical Sciences, University of Delaware, Newark, DE 19716, USA

June 11, 2025

Abstract

In this paper, we propose a novel adaptive-rank method for simulating multi-scale BGK equations which is based on a greedy sampling technique. The method adaptively identifies important rows and columns of the solution matrix, and reduces computational complexity by updating only the selected rows and columns through a local solver. Once updated, the solution at selected rows and columns is used together with an adaptive cross approximation to reconstruct the entire solution matrix. The approach extends the semi-Lagrangian adaptive-rank approach, introduced in our previous work for the Vlasov-Poisson system [39] in several ways. Unlike the step-and-truncate low-rank integrators discussed in [13], the greedy sampling technique considered in this paper avoids the need for explicit low-rank decompositions of nonlinear terms, such as the local Maxwellian in the BGK collision operator. We enforce mass, momentum, and energy conservation by introducing a new locally macroscopic conservative correction, which implicitly couples the kinetic solution to the solution of the corresponding macroscopic system. Using asymptotic analysis, we show that the macroscopic correction preserves the asymptotic properties intrinsic to the full-grid scheme and that the proposed method in the low-rank setting possesses a conditionally asymptotic-preserving property. Another unique advantage of our approach is the use of a local semi-Lagrangian solver, which permits large time steps compared to Eulerian schemes. This flexibility is retained in the macroscopic solver by employing high-order stiffly-accurate diagonally implicit Runge-Kutta methods. The resulting nonlinear macroscopic systems are solved efficiently using a Jacobian-free Newton-Krylov method, which eliminates the need for preconditioning at modest CFL numbers. Each iteration of the nonlinear macroscopic solver provides a self-consistent correction to a provisional low-rank kinetic solution, which is then used as a dynamic closure for the macroscopic system. Numerical results demonstrate the efficacy of the proposed method in capturing shocks and discontinuous solution structures. We also highlight its performance in a challenging mixed-regime problem, where the Knudsen number spans multiple orders of magnitude.

Keywords: Sampling, adaptive-rank, cross approximation, multi-scale methods, BGK equation, conservation laws

^{*}wsands@udel.edu

[†]jingqiu@udel.edu

[‡]dphayes@udel.edu

[§]Corresponding author: nyzheng@udel.edu

1 Introduction

The Bhatnagar–Gross–Krook (BGK) equation [3] is a popular model used to study the dynamics of rarefied gases when the mean-free path is large compared to characteristic length scales, causing fluid models such as the Euler and Navier Stokes equations to break down. It is a nonlinear relaxation model that approximates the collision dynamics of the well-known Boltzmann collision operator which requires the evaluation of a five-dimensional integral that is prohibitively expensive due to its intrinsic nonlinearity and high-dimensionality. In contrast, the BGK operator is a simpler nonlinear algebraic operator; yet it retains key properties of the Boltzmann operator, such as entropy dissipation and the preservation of collision invariants (e.g., mass, momentum, and energy) and various multiscale phenomena. As a result, the BGK equation serves as a valuable prototype for studying more complex collision operators.

Low-rank tensor approximations in the context of kinetic simulations have attracted significant interest in recent years [13]. Such methods compress the time-dependent numerical solution using low-rank decomposition techniques developed for matrices and tensors, and are a promising tool to address the challenges associated with the curse of dimensionality. The primary research directions in this area can be interpreted as either dynamic low-rank (DLR) or step-and-truncate (SAT) methods. DLR methods [25, 14, 11, 12, 4, 2] project the continuous equation onto a low-rank manifold using the low-rank bases from the solution, and then discretize the resulting equations to obtain evolution equations for the bases. In contrast, SAT methods [26, 9, 16, 15, 33] first discretize the kinetic equation and dynamically evolve a low-rank representation of the solution using tensor linear algebra. One of the challenges associated with the BGK collision operator in the context of low-rank methods is the need to evaluate a local Maxwellian, which generally does not admit a low-rank decomposition. To avoid these challenges, some of the existing low-rank methods for the BGK equation in the DLR [12, 2] framework use a multiplicative splitting that is guided by the structure of the solution obtained from Chapman-Enskog analysis. Interpolatory low-rank methods, also known as CUR or cross approximation [34], or an oblique projection in the DLR framework [7, 8], employ a sampling strategy based on the discrete empirical interpolation method (DEIM) that allows one to avoid forming explicit low-rank decompositions. This is particularly advantageous for the evaluation of the local Maxwellian in the BGK equation, where such methods were recently used to investigate compression of the entire six-dimensional distribution function [8]. In a recent work [39], the adaptive cross approximation of matrices [34] was used to construct a non-split semi-Lagrangian adaptive-rank (SLAR) method that was applied to the nonlinear Vlasov-Poisson system [39]. Compared with existing low-rank approaches, the sampling-based adaptive-rank methods uses information from a residual to adaptively identify critical rows and columns that need to be updated. Once the rows and columns are identified, the low-rank approximation is then updated using low-cost recursive rank-one corrections. These rows and columns are a subset of the entire matrices, with a computational complexity similar to that of a low-rank solver. The method is also demonstrated to be highly flexible in the development of numerical schemes, can achieve high-order convergence in spatial and temporal discretizations, and can achieve the mass conservation property via a locally macroscopic conservation (LoMaC) type correction, similar to those in [15, 17].

The goal of this work is to develop a new adaptive-rank approach for the multi-scale BGK equation that employs a greedy sampling strategy. The local solver used in this work is built upon a SL finite difference method [27], which achieves high-order accuracy in both temporal and spatial discretizations and allows for rather large time steps with numerical stability. In [10], such a local solver was shown to be asymptotic preserving (AP) and asymptotically accurate (AA) for the BGK equation in the semi-discrete sense. This work is built upon such a local

solver, but with the greedy sampling technique and the SLAR method from our recent work [39], which was shown to be flexible in its implementation, robust in its numerical performance, and efficient with a low-rank complexity. A key advantage of the adaptive-rank approach considered in this work is that explicit low-rank decomposition of local Maxwellians are no longer necessary, which greatly simplifies the construction of low-rank solvers for the BGK equation. This work also introduces a new LoMaC correction which can simultaneously achieve mass, momentum, and energy conservation. The original version of LoMaC proposed in [15] considered explicit schemes for the macroscopic system. To eliminate the CFL restriction from the macroscopic system, we consider implicit discretizations that couple the macroscopic and microscopic systems in order to define a dynamic and self-consistent correction of the low-rank kinetic solution. The approach we use is inspired by HOLO methods [36, 35, 30, 18] which have shown great success in the simulation of highly nonlinear kinetic problems. At its core, the HOLO method uses a macroscopic (moment) formulation with a dynamic closure to accelerate the convergence of a nonlinear scheme for the kinetic equation. The nonlinear schemes for the kinetic equation are often linearized using Picard iteration, which requires one to solve the kinetic equation multiple times. In contrast, the approach we present first computes a high quality provisional low-rank solution with a non-conservative SL method. Then, using a nonlinear iterative method, we simultaneously correct the provisional solution in a way that directly enforces the macroscopic conservation laws. In order to retain the efficiency of the SL method, we discretize the macroscopic equations using high-order stiffly-accurate (SA) diagonally-implicit Runge-Kutta (DIRK) methods. The resulting nonlinear systems are solved using a Jacobian-free Newton-Krylov (JFNK) method, which, for modest CFL, does not require preconditioning and uses the high-quality non-conservative provisional solution as an initial guess. We also would like to remark that the proposed LoMaC approach is quite general and does not require a low-rank decomposition of nonlinear terms.

The organization of the paper is structured as follows. First in Section 2, we introduce the kinetic model and its associated macroscopic system. The bulk of this paper is concentrated in Section 3 and subsections therein. We provide a brief overview of the high-order SL finite difference method for the BGK equation [27] in Section 3.1, which is the full rank version of the proposed adaptive-rank method described in Section 3.2. In Section 3.3, we provide details regarding the preservation of the macroscopic conservation laws, and discuss the techniques used to solve the coupled nonlinear macroscopic system. Section 3.4 describes extensions of the aforementioned methods to high-order temporal accuracy using DIRK. We also conduct an asymptotic analysis of the method near the fluid limit and prove that the scheme possesses a *conditionally* AP property. Numerical results are provided in Section 4 to confirm the accuracy and robustness of the proposed methodologies. Section 5 contains the conclusion, which provides an overview of the results and discusses extensions for future work.

2 The Multi-scale Kinetic Equation and Macroscopic System

In this section, we provide details of the models that will be investigated in this work as well as the conventions used regarding notation. We first introduce the kinetic model in Section 2.1 and discuss its corresponding macroscopic system in Section 2.2.

2.1 The BGK Equation

We consider the BGK relaxation model [3] of the Boltzmann equation, which, for neutral particles, in the absence of external forces, leads to the kinetic model

$$f_t + v f_x = \frac{\mathcal{M}_{\mathbf{U}(f)} - f}{\epsilon}, \quad (x, v) \in \Omega_x \times \Omega_v. \quad (2.1)$$

Here, the distribution function $f = f(x, v, t)$ represents the probability of finding a particle at position $x \in \Omega_x$, with velocity $v \in \Omega_v$, at time t . The parameter $\epsilon > 0$ is the Knudsen number whose inverse characterizes the relaxation rate of the system to its local thermodynamic equilibrium. As a consequence of the Boltzmann \mathcal{H} -theorem, this equilibrium is defined to be the local Maxwellian distribution

$$\mathcal{M}_{\mathbf{U}(f)} := \frac{\rho}{\sqrt{2\pi T}} \exp\left(-\frac{(v-u)^2}{2T}\right), \quad (2.2)$$

where we have defined the raw moments

$$\rho = \langle f \rangle_v, \quad \rho u = \langle v f \rangle_v, \quad E = \left\langle \frac{1}{2} v^2 f \right\rangle_v, \quad \mathbf{U}(f) := \begin{pmatrix} \rho \\ \rho u \\ E \end{pmatrix}, \quad (2.3)$$

as well as the central moment

$$\frac{\rho T}{2} = \left\langle \frac{1}{2} (v-u)^2 f \right\rangle_v. \quad (2.4)$$

To simplify the notation, we write

$$\langle g \rangle_v := \int_{\Omega_v} g(x, v, t) dv, \quad (2.5)$$

to denote integration of a function $g = g(x, v, t)$ in velocity. It is useful to note that the total energy density E can be written in terms of the bulk kinetic energy and internal energy, namely

$$E = \frac{1}{2} (\rho u^2 + \rho T). \quad (2.6)$$

Finally, an important property of the BGK collision operator is that it possesses several invariants. In particular, it preserves mass, momentum, and energy in the sense that

$$\left\langle \left(\frac{\mathcal{M}_{\mathbf{U}(f)} - f}{\epsilon} \right) \Phi \right\rangle_v = 0, \quad \Phi(v) = \left(1, v, \frac{1}{2} v^2 \right)^\top. \quad (2.7)$$

2.2 Macroscopic System

In addition to the kinetic equation (2.1), this work also utilizes the conserved macroscopic system, which is obtained in a self-consistent manner through moments of the distribution function f . This system of moment equations can be obtained from (2.1) by multiplying both sides with a function $\Phi(v) = \left(1, v, \frac{1}{2} v^2 \right)^\top$ and then applying the operator $\langle \cdot \rangle_v$ to both sides. By (2.7), the functions in $\Phi(v)$ are known to be collision invariants, so we obtain a system for the macroscopic variables of the form

$$\mathbf{U}_t + \mathbf{F}(\mathbf{U})_x = 0, \quad (2.8)$$

where the conserved quantities $\mathbf{U} = \mathbf{U}(f)$ are defined according to (2.3), and the macroscopic flux $\mathbf{F}(\mathbf{U})$ can be written as

$$\mathbf{F}(\mathbf{U}) := \begin{pmatrix} \langle vf \rangle_v \\ \langle v^2 f \rangle_v \\ \langle \frac{1}{2} v^3 f \rangle_v \end{pmatrix}. \quad (2.9)$$

We remark that the macroscopic flux (2.9) can be equivalently written in terms of the conserved variables \mathbf{U} , with the flux of the last equation requiring a closure. The structure of the system (2.8) characterizes the fluid limit of the kinetic equation in the limit $\epsilon \rightarrow 0$, which should be preserved at the discrete level. In particular, as $\epsilon \rightarrow 0$, the distribution can be well-approximated by a local Maxwellian. A standard perturbation argument shows that $f = \mathcal{M}_{\mathbf{U}(f)}$ to leading order in ϵ , which results in the compressible Euler system, if it is used as the closure. Corrections to $\mathcal{O}(\epsilon)$ and beyond can be achieved using the classical Chapman-Enskog expansion [5], leading to the Navier-Stokes and Burnett equations. In this work, we take a slightly different approach in which an approximate solution of the kinetic equation defines the closure of the moment system. This approximate solution shall be obtained using the adaptive-rank method described in the following section, which is developed using a greedy sampling technique. A critical aspect of our approach is that the solution of the moment system is treated in a manner that is self-consistent with the kinetic equation. This, in turn, allows us to simultaneously satisfy key conservation laws and preserve the structure of the fluid limit. We provide additional details of this technique in Section 3.3.

3 Adaptive-rank Method and Preservation of Conservation Laws

We begin with a brief review of high-order deterministic (full-rank) SL-FD methods for the BGK equation in Section 3.1. Then, in Section 3.2 and Section 3.3, we describe the proposed sampling-based adaptive-rank method and the iterative procedure used to enforce macroscopic conservation laws. These methods are all developed under a first-order backward Euler time discretization to highlight the key algorithmic ideas. In Section 3.4, we extend the approach to high-order accuracy in time using stiffly-accurate DIRK methods. Finally, in Section 3.5, we perform an asymptotic analysis of the proposed scheme.

3.1 SL-FD Method for the BGK Equation

In this paper, we discretize the phase space $\Omega_x \times \Omega_v = [a_x, b_x] \times [a_v, b_v]$ with a uniform Cartesian mesh consisting of $N_x \times N_v$ cells whose boundaries are

$$\begin{aligned} a_x &= x_{\frac{1}{2}} < x_{\frac{3}{2}} < \dots < x_{N_x + \frac{1}{2}} = b_x, \\ a_v &= v_{\frac{1}{2}} < v_{\frac{3}{2}} < \dots < v_{N_v + \frac{1}{2}} = b_v. \end{aligned}$$

For brevity, we denote the cells, as well as their respective centers and resolutions, as

$$\begin{aligned} I_i^x &= [x_{i-\frac{1}{2}}, x_{i+\frac{1}{2}}], \quad x_i = \frac{1}{2}(x_{i-\frac{1}{2}} + x_{i+\frac{1}{2}}), \quad \Delta x = x_{i+\frac{1}{2}} - x_{i-\frac{1}{2}}, \quad \text{for } i = 1, \dots, N_x, \\ I_j^v &= [v_{j-\frac{1}{2}}, v_{j+\frac{1}{2}}], \quad v_j = \frac{1}{2}(v_{j-\frac{1}{2}} + v_{j+\frac{1}{2}}), \quad \Delta v = v_{j+\frac{1}{2}} - v_{j-\frac{1}{2}}, \quad \text{for } j = 1, \dots, N_v. \end{aligned}$$

It is also convenient to write $I_{i,j} = I_i^x \times I_j^v$ for all i, j when referring to cells in the two-dimensional grid. Lastly, we can organize the cell centers into vectors, namely

$$\mathbf{x} := [x_1, x_2, \dots, x_{N_x}]^\top, \quad \mathbf{v} := [v_1, v_2, \dots, v_{N_v}]^\top.$$

Next, using the material derivative, we cast the BGK equation (2.1) in terms of its characteristics, which gives

$$\frac{df}{dt} = f_t + v f_x = \frac{\mathcal{M}_{\mathbf{U}(f)} - f}{\epsilon}. \quad (3.1)$$

A first-order backward Euler (BE) time discretization along these characteristics produces

$$\begin{aligned} f_{i,j}^{n+1} &= f(x_i - v_j \Delta t, v_j, t^n) + \Delta t \frac{(\mathcal{M}_{\mathbf{U}(f^{n+1}))_{i,j}} - f_{i,j}^{n+1}}{\epsilon}, \\ &=: \tilde{f}_{i,j}^{n+1} + \Delta t \frac{(\mathcal{M}_{\mathbf{U}(\tilde{f}^{n+1}))_{i,j}} - \tilde{f}_{i,j}^{n+1}}{\epsilon}. \end{aligned} \quad (3.2)$$

Next, if we multiply both sides of the update (3.2) by $\Phi(v) = (1, v, \frac{1}{2}v^2)^\top$, and apply the operator $\langle \cdot \rangle_v$, with the aid of property (2.7), it can be shown that

$$\mathcal{M}_{\mathbf{U}(f^{n+1})} = \mathcal{M}_{\mathbf{U}(\tilde{f}^{n+1})}. \quad (3.3)$$

Hence, the BE time discretization (3.2) can be rewritten in an explicit form:

$$f_{i,j}^{n+1} = \frac{\epsilon \tilde{f}_{i,j}^{n+1} + \Delta t (\mathcal{M}_{\mathbf{U}(\tilde{f}^{n+1}))_{i,j}}}{\epsilon + \Delta t}. \quad (3.4)$$

To perform the spatial reconstruction of $\tilde{f}_{i,j}^{n+1}$ from the feet of characteristics as in Equation (3.2), we use the fifth-order finite difference scheme combined with WENO reconstructions [27]. This BE discretization of the BGK equation was previously shown to be AP and was extended to high order using DIRK methods [10] with the AA property. In Section 3.5, we extend these ideas to account for the truncation process used in low-rank approximation. As outlined above, we begin by presenting the method under a first-order backward Euler discretization, which serves as the foundation for the adaptive-rank scheme. The extension to high-order accuracy using DIRK methods is discussed separately in Section 3.4.

3.2 An Adaptive-rank Method for the BGK Equation with Greedy Sampling

To elaborate the idea of the adaptive-rank approach with greedy sampling, we adopt the following notation for the solution matrices $F^n = (f_{i,j}^n)_{N_x \times N_v}$ and the intermediate solution $\tilde{F}^{n+1} = (\tilde{f}_{i,j}^{n+1})_{N_x \times N_v}$ from the SL update. The element-wise update in (3.4) can be rewritten in matrix form as

$$F^{n+1} := \mathbf{L}(\tilde{F}^{n+1}) = \mathbf{L} \circ \mathbf{S}(F^n), \quad (3.5)$$

where \mathbf{S} represents the SL method with reconstruction [27], and \mathbf{L} denotes the nonlinear update operator defined in (3.4). We next describe the adaptive-rank compression strategy used to efficiently represent each operator in this composition.

ACA+SVD Strategy

The core compression routine used in our adaptive-rank framework is a two-stage strategy that combines the adaptive cross approximation (ACA) with an SVD truncation. This ACA+SVD strategy, originally proposed as the central component of the SLAR method in our previous work [39], enables efficient construction of low-rank approximations using only a subset of matrix entries. The ACA is particularly well-suited for problems where operators, solution updates, or nonlinear terms can

be evaluated locally without assembling the full matrix. The subsequent SVD truncation further enhances the robustness of the method by reducing redundancy and improving numerical stability [39]. We briefly recall the ACA+SVD strategy below, beginning with a visual illustration of the CUR decomposition.

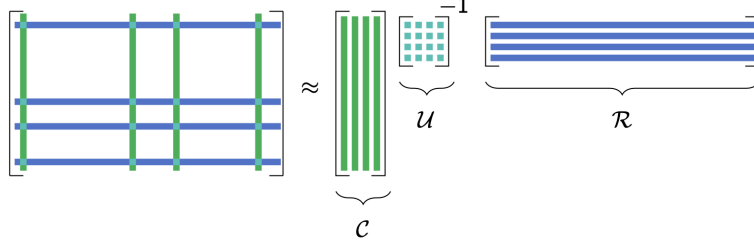


Figure 3.1: Visual representation of the CUR decomposition constructed by ACA.

Given a matrix $A \in \mathbb{C}^{N_x \times N_v}$, the ACA algorithm provides an efficient way to construct a CUR decomposition (see Figure 3.1) of the form

$$A_k = A(:, \mathcal{J}) A(\mathcal{I}, \mathcal{J})^{-1} A(\mathcal{I}, :) =: \mathcal{C} \mathcal{U} \mathcal{R}, \quad (3.6)$$

where $\mathcal{I} = \{i_1, i_2, \dots, i_k\}$ and $\mathcal{J} = \{j_1, j_2, \dots, j_k\}$ are the selected row and column index sets; \mathcal{C} and \mathcal{R} denote the corresponding selected columns and rows of A , and \mathcal{U} is the inverse of the intersection matrix $A(\mathcal{I}, \mathcal{J})$. While choosing the optimal index set in a CUR decomposition is NP-hard [6], ACA builds up the decomposition using a greedy pivoting strategy driven by residual error.

The recursive ACA algorithm [34, 39] constructs the approximation iteratively by updating a rank- k representation via a rank-one correction to the previous rank- $k - 1$ approximation. Each iteration—referred to as the k -th step—proceeds as follows:

Phase I: Pivot selection. Let A_{k-1} denote the current approximation (with $A_0 = (0)_{N_x \times N_v}$) and $R_{k-1} = A - A_{k-1}$ the corresponding residual. At iteration k , a candidate set of index pairs $\mathcal{P} = \{(i_\ell, j_\ell)\}_{\ell=1}^{12}$ is randomly sampled from the unselected rows and columns. The pivot location is initialized as $(i^*, j^*) = \arg \max_{(i,j) \in \mathcal{P}} |R_{k-1}(i, j)|$, followed by greedy refinement steps:

$$i_k = \arg \max_i |R_{k-1}(i, j^*)|, \quad j_k = \arg \max_j |R_{k-1}(i_k, j)|.$$

The pair (i_k, j_k) is then appended to the index sets \mathcal{I} and \mathcal{J} .

Phase II: Rank-one update. A rank-one correction is applied:

$$A_k = A_{k-1} + \frac{1}{R_{k-1}(i_k, j_k)} R_{k-1}(:, j_k) R_{k-1}(i_k, :). \quad (3.7)$$

This update is equivalent to the standard CUR decomposition (3.6), which ensures interpolation at all selected rows and columns in \mathcal{I} and \mathcal{J} : the updated approximation satisfies $A_k(i_\ell, :) = A(i_\ell, :)$, $A_k(:, j_\ell) = A(:, j_\ell)$ for $\ell = 1, \dots, k$. This process continues until the Frobenius norm of the most recent rank-one correction falls below a prescribed tolerance ε_c , or until a specified maximum rank is reached.

The resulting ACA approximation admits a structured decomposition:

$$A_k = \mathcal{E}_{\mathcal{J}} \mathcal{D} \mathcal{E}_{\mathcal{I}},$$

where $\mathcal{E}_{\mathcal{J}} = [\mathbf{c}_1, \dots, \mathbf{c}_k]$ with $\mathbf{c}_\ell = R_{\ell-1}(:, j_\ell)$; $\mathcal{E}_{\mathcal{I}} = [\mathbf{r}_1, \dots, \mathbf{r}_k]^T$ with $\mathbf{r}_\ell = R_{\ell-1}(i_\ell, :)^T$; and $\mathcal{D} = \text{diag}(r_1^{-1}, \dots, r_k^{-1})$ with $r_\ell = R_{\ell-1}(i_\ell, j_\ell)$.

SVD truncation. To improve numerical stability and eliminate redundant modes, the CUR approximation is further compressed using singular value decomposition (SVD). Specifically, we first perform QR decompositions of $\mathcal{E}_{\mathcal{J}}$ and $\mathcal{E}_{\mathcal{I}}^T$, followed by an SVD on the reduced core:

$$\mathcal{E}_{\mathcal{J}} = Q_1 R_1, \quad \mathcal{E}_{\mathcal{I}}^T = Q_2 R_2, \quad R_1 D R_2^T = \tilde{U} \tilde{\Sigma} \tilde{V}^T.$$

We then truncate the decomposition at rank r_s , defined by the smallest integer such that $\tilde{\Sigma}(r_s + 1, r_s + 1) < \varepsilon_s$, and construct the final approximation:

$$A \approx \left(Q_1 \tilde{U}(:, 1:r_s) \right) \tilde{\Sigma}(1:r_s, 1:r_s) \left(Q_2 \tilde{V}(:, 1:r_s) \right)^T =: U \Sigma V^T,$$

which defines the final output format of the ACA+SVD strategy.

We now apply this compression strategy to the BGK update operator. Using the formulation (3.5), we define the corresponding low-rank approximation as

$$\mathcal{F}^{n+1,\star} = \mathcal{L} \circ \mathcal{S}(\mathcal{F}^n), \quad (3.8)$$

where $\mathcal{S} := \mathcal{T}_{\varepsilon_s} \circ \mathcal{S}_{\varepsilon_c}$ and $\mathcal{L} := \mathcal{T}_{\varepsilon_s} \circ \mathcal{L}_{\varepsilon_c}$ represent two ACA+SVD stages used to approximate the SL update operator \mathbf{S} and the nonlinear collision operator \mathbf{L} , respectively. The superscript \star in $\mathcal{F}^{n+1,\star}$ indicates that this intermediate result does not yet satisfy local conservation laws. The LoMaC correction procedure, introduced later in Section 3.3, will adjust $\mathcal{F}^{n+1,\star}$ to enforce conservation of mass, momentum, and energy, yielding the final conservative solution \mathcal{F}^{n+1} .

Figure 3.2 illustrates the full adaptive-rank update procedure at each BE step. From bottom to top, the five layers are interpreted as follows. The process begins with the solution \mathcal{F}^n at the current time level. The operator $\mathcal{S}_{\varepsilon_c}$ applies the ACA algorithm with sampling threshold ε_c , performing local SL characteristic tracing and spatial reconstruction at the feet of the characteristics. This yields a CUR approximation of rank k_1 , denoted $\tilde{\mathcal{F}}_{\{\#,k_1\}}^{n+1}$. Applying SVD truncation with tolerance ε_s via $\mathcal{T}_{\varepsilon_s}$, we obtain a rank- r_1 approximation $\tilde{\mathcal{F}}_{\{\#,k_1 \rightarrow r_1\}}^{n+1}$. Next, the operator $\mathcal{L}_{\varepsilon_c}$ performs ACA again, now acting entry-wise on the nonlinear update operator as defined in (3.4), producing a rank- k_2 approximation $\mathcal{F}_{\{\#,k_2\}}^{n+1,\star}$. Another SVD truncation reduces it to rank r_2 , yielding $\mathcal{F}_{\{\#,k_2 \rightarrow r_2\}}^{n+1,\star}$. Finally, the LoMaC correction step is applied to restore conservation properties, resulting in the final low-rank solution \mathcal{F}^{n+1} .

The ACA+SVD strategy serves as a general compression framework that extends beyond the current setting. It is applicable to a broad class of problems where operators, solution updates, or nonlinear terms can be accessed locally without requiring full matrix assembly. This includes constructing adaptive-rank solvers for local time-stepping schemes, and developing compressed representations for nonlinear update formulas such as (3.4). In particular, when ACA+SVD is applied to a local SL solver, the resulting operator reduces to the SLAR formulation proposed in our earlier work. The operator \mathcal{S} in this paper can thus be regarded as an instance of the SLAR method.

3.3 Preservation of Macroscopic Conservation Laws

In our previous work [39], we ensured mass conservation in the SLAR method by simultaneously solving a macroscopic equation for the charge density, in a manner inspired by the LoMaC framework [15]. A notable advantage of the SL method is its ability to take large time steps, which we preserved by discretizing the macroscopic equation with an implicit method. This resulted in a linear system for the charge density whose solution was used to correct the total mass of the distribution. In this work, we further extend this technique to simultaneously achieve mass, momentum,

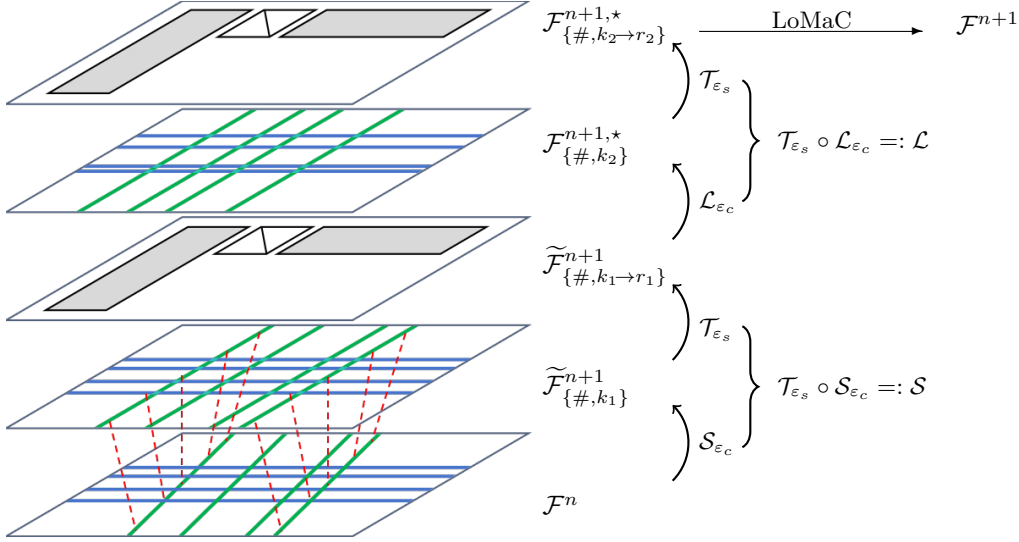


Figure 3.2: Adaptive-rank method for the BGK equation.

and energy conservation by implicitly solving a nonlinear system. In the following, we propose a nonlinear implicit solver for the macroscopic system; the updated macroscopic observables serve as constraints for correcting the low-rank solution, thereby ensuring local conservation of mass, momentum, and energy.

To demonstrate the idea, we consider a first-order BE time discretization, which offers a natural extension to high-order using DIRK methods. The process starts from a provisional non-conservative kinetic solution $f^{n+1,*}$ obtained with the BE method (3.4), which will be corrected to obtain a conservative solution. Motivated by property (2.7), we seek a *conservative kinetic solution* with the following LoMaC correction format:

$$f^{n+1}(\mathbf{U}^{n+1}) = f^{n+1,*} - \mathcal{M}_{\mathbf{U}(f^{n+1,*})} + \mathcal{M}_{\mathbf{U}^{n+1}}. \quad (3.9)$$

Here, $\mathcal{M}_{\mathbf{U}^{n+1}}$ is the local Maxwellian constructed from \mathbf{U}^{n+1} , where \mathbf{U}^{n+1} is obtained by solving the following macroscopic fluid system with a BE discretization

$$\mathbf{U}^{n+1} = \mathbf{U}^n - \Delta t \mathbf{F}(\mathbf{U}^{n+1})_x, \quad (3.10)$$

whose flux is *implicitly* defined using the moments of the kinetic solution (3.9), namely

$$\mathbf{F}(\mathbf{U}^{n+1}) := \left\langle \begin{pmatrix} f^{n+1}v \\ f^{n+1}v^2 \\ f^{n+1}(\frac{1}{2}v^3) \end{pmatrix} \right\rangle_v. \quad (3.11)$$

Using the definition (3.9), we can equivalently express the flux (3.11) as

$$\mathbf{F}(\mathbf{U}^{n+1}) := \left\langle [f^{n+1,*} - \mathcal{M}_{\mathbf{U}(f^{n+1,*})}] \begin{pmatrix} 0 \\ 0 \\ \frac{1}{2}v^3 \end{pmatrix} \right\rangle_v + \left\langle \mathcal{M}_{\mathbf{U}^{n+1}} \begin{pmatrix} v \\ v^2 \\ \frac{1}{2}v^3 \end{pmatrix} \right\rangle_v. \quad (3.12)$$

It is important to note that the first term on the right-hand side of (3.12) is fixed with respect to \mathbf{U}^{n+1} . In addition, the nonlinear dependence on \mathbf{U}^{n+1} is entirely captured in the second term, which means that the non-conservative kinetic solution $f^{n+1,*}$ is only used to initialize the closure of the fluid system. We then apply an iterative method that dynamically updates the macroscopic closure based on the current moments until convergence is achieved. Then the moments are used to correct the kinetic solution with the LoMaC correction formula (3.9). Figure 3.3 illustrates one step of the proposed method with the BE discretization, including the LoMaC correction loop, which is shown using solid lines. Here dashed lines indicate that the kinetic solver is isolated from this process. Further details regarding the numerical treatment of this nonlinear system are provided in the following subsections.

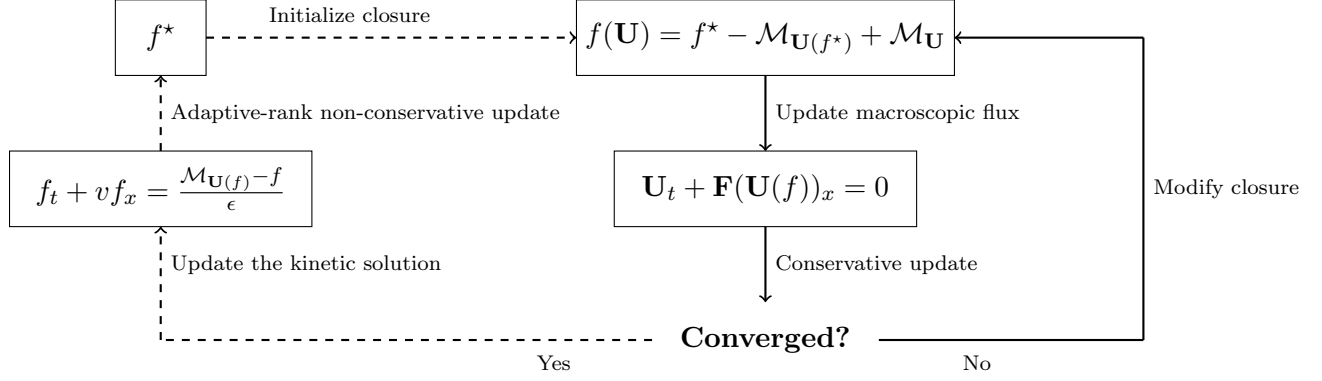


Figure 3.3: A flowchart of the proposed algorithm for the BGK equation with the LoMaC correction.

3.3.1 Spatial Discretization of the Nonlinear system

There are many conservative spatial discretizations available for approximating the macroscopic system. To obtain a fully discrete method for (3.10) based on the BE method, we combine an upwind flux-splitting method with a high-order reconstruction technique. This combination produces a high-order conservative approximation to the spatial derivative, which we write as

$$\mathbf{U}_i^{n+1} = \mathbf{U}_i^n - \frac{\Delta t}{\Delta x} \left(\hat{\mathbf{F}}_{i+\frac{1}{2}}^{n+1} - \hat{\mathbf{F}}_{i-\frac{1}{2}}^{n+1} \right). \quad (3.13)$$

Here, the numerical fluxes $\hat{\mathbf{F}}_{i\pm\frac{1}{2}}^{n+1}$ for the macroscopic system are defined using a kinetic flux vector splitting (KFVS) technique [28, 38], which separates the velocity domain into positive and negative components, corresponding to particle motion in different directions. This provides the correct wind directions needed to perform high-order spatial reconstruction methods. In KFVS, we express the flux as $\hat{\mathbf{F}}^{n+1} = \hat{\mathbf{F}}^{n+1,+} + \hat{\mathbf{F}}^{n+1,-}$, where the split fluxes used in the reconstructions are given by

$$\hat{\mathbf{F}}^{n+1,\pm} = \widetilde{\int_{\mathbb{R}^{\pm}}} f^{n+1} \begin{pmatrix} v \\ v^2 \\ \frac{1}{2}v^3 \end{pmatrix} dv. \quad (3.14)$$

Here, $\widetilde{\int_{\mathbb{R}^{\pm}}} \cdot dv$ denotes a low-rank numerical integration over the half-real velocity domains, as described in Appendix A. Once the split flux stencil values are obtained from (3.14), a high-order

reconstruction is applied to evaluate the fluxes at cell interfaces. In this work, we use the fifth-order classical WENO-JS reconstructions [20], which are written as

$$\begin{aligned}\widehat{\mathbf{F}}_{i+\frac{1}{2}}^{n+1} &= \widehat{\mathbf{F}}_{i+\frac{1}{2}}^{n+1,+} + \widehat{\mathbf{F}}_{i+\frac{1}{2}}^{n+1,-} \\ &:= \mathcal{R}^+ \left(\left\{ \mathbf{F}_{i-2}^{n+1,+}, \dots, \mathbf{F}_{i+2}^{n+1,+} \right\} \right) + \mathcal{R}^- \left(\left\{ \mathbf{F}_{i-1}^{n+1,-}, \dots, \mathbf{F}_{i+3}^{n+1,-} \right\} \right).\end{aligned}\quad (3.15)$$

Here, we use \mathcal{R}^\pm to denote the WENO reconstructions of the flux at a cell interface.

Spatial discretization of (3.13) results in a system of nonlinear algebraic equations for the discrete macroscopic variables \mathbf{U}^{n+1} , which can be written in the form

$$\mathbf{G}(\mathbf{U}^{n+1}) = 0. \quad (3.16)$$

An important observation is that the size of the resulting nonlinear problem scales with the size of the system for the macroscopic variables and *not* the kinetic equation. In other words, it is of reduced dimensionality.

3.3.2 Newton-Krylov Methods for the Nonlinear System

In the previous section, we found that the implicit, fully-discrete macroscopic system for the BGK equation with the dynamic closure leads to a nonlinear system of the form

$$\mathbf{G}(\mathbf{U}) = 0, \quad (3.17)$$

where we have dropped the reference to the time level, for brevity. A Newton method for (3.17) uses the linearization about a current iterate $\mathbf{U}^{(k)}$, resulting in the sequence of linear systems

$$J^{(k)} \delta \mathbf{U}^{(k)} = -\mathbf{G}(\mathbf{U}^{(k)}), \quad \text{for } k = 1, 2, \dots, \quad (3.18)$$

where $J^{(k)} = \mathbf{G}'(\mathbf{U}^{(k)})$ is the Jacobian matrix of the system evaluated at the current iterate and $\delta \mathbf{U}^{(k)}$ is the correction to $\mathbf{U}^{(k)}$. After solving (3.18) for the correction $\delta \mathbf{U}^{(k)}$, we obtain the updated state

$$\mathbf{U}^{(k+1)} = \mathbf{U}^{(k)} + \delta \mathbf{U}^{(k)}. \quad (3.19)$$

As discussed at the end of the previous section, the size of this nonlinear system depends entirely on the size of the problem for the macroscopic system. In the more general setting, the system will be of size $M_d N^d \times M_d N^d$, where N is the number of cells per spatial dimension, $d = 1, 2, 3$, and M_d is the number of conserved quantities with dimension d . Other complications arise due to the use of nonlinear spatial reconstruction methods in the macroscopic solver and its nonlinear coupling to the solution from the kinetic solver. These features make analytical evaluations of the Jacobian expensive.

Instead, we consider Newton-Krylov methods, which typically combine an inexact Newton method with Krylov subspace methods. Inexact Newton methods use an approximation of the Jacobian, which slightly weakens its convergence rate compared to an exact Newton method. However, the adaptive-rank kinetic solver we employ provides a high-quality, inexpensive initial guess for the Newton method that is non-conservative. A notable advantage of inexact Newton methods is that they can be used in an entirely matrix-free setting and are known as Jacobian-free Newton-Krylov methods [22, 23]. In particular, products between the Jacobian matrix $J^{(k)}$ and an arbitrary vector \mathbf{V} can be approximated as

$$J^{(k)} \mathbf{V} = \frac{\mathbf{G}(\mathbf{U}^{(k)} + \epsilon \mathbf{V}) - \mathbf{G}(\mathbf{U}^{(k)})}{\epsilon} + \mathcal{O}(\epsilon), \quad (3.20)$$

without ever explicitly forming a Jacobian matrix. Here the parameter $\epsilon > 0$ (different from the Knudsen number) defines a perturbation of the current state $\mathbf{U}^{(k)}$, with the error being proportional to ϵ . This approximation avoids the explicit formation of the Jacobian matrix. Consequently, it naturally motivates the use of Krylov subspace methods, in particular GMRES, which search for a solution to the linear systems (3.18) using the subspaces spanned by recursive Jacobian-vector products.

3.4 Extensions to High-order using Runge-Kutta Methods

To obtain higher-order temporal accuracy, we apply high-order DIRK methods [1, 21]. The Butcher

tableau for a DIRK method is given by $\begin{array}{c|c} \mathbf{c} & A \\ \hline & \mathbf{b}^T \end{array}$, where $A = (a_{i,j}) \in \mathbb{R}^{s \times s}$ is an invertible lower triangular matrix, $\mathbf{c} = [c_1, \dots, c_s]^\top$ is the intermediate coefficient vector, and $\mathbf{b}^\top = [b_1, \dots, b_s]$ represents the quadrature weights. In order to address the stiffness in (2.1) when $\epsilon \ll 1$, we use DIRK methods with the SA property, for which $A(s, :) = \mathbf{b}^\top$ and $f^{n+1} = f^{(s)}$.

The SL-FD method from our previous work [27] applies DIRK methods along the characteristics, so that the solution at internal stages $f^{(k)}$ is given by

$$\begin{aligned} f_{i,j}^{(k)} &= f^n(x_i - v_j c_k \Delta t, v_j) + \Delta t \sum_{\ell=1}^k a_{k,\ell} \left(\frac{\mathcal{M}_{\mathbf{U}(f^{(\ell)})} - f^{(\ell)}}{\epsilon} \right) (x_i - v_j (c_k - c_\ell) \Delta t, v_j) \\ &=: \tilde{f}^{(k)} + a_{k,k} \Delta t \left(\frac{\mathcal{M}_{\mathbf{U}(f^{(k)})} - f^{(k)}}{\epsilon} \right) (x_i, v_j), \quad \text{for } k = 1, \dots, s. \end{aligned} \quad (3.21)$$

The implicit advance (3.21) at each stage can be written in an explicit form, similar to the BE discretization (3.4), which leads to the stage-wise update

$$f_{i,j}^{(k)} = \frac{\epsilon \tilde{f}_{i,j}^{(k)} + a_{k,k} \Delta t \left(\mathcal{M}_{\mathbf{U}(\tilde{f}^{(k)})} \right)_{i,j}}{\epsilon + a_{k,k} \Delta t}, \quad \text{for } k = 1, \dots, s. \quad (3.22)$$

As a consequence of the SA property, it follows that $f^{n+1} = f^{(s)}$. Additionally, we note that there is an alternative approach to evaluating the intermediate solutions $\tilde{f}^{(k)}$ in (3.22), known as the Shu-Osher form [10]. In this study, we adopt the Shu-Osher form as it proved more reliable for simulations involving discontinuous solutions.

High-order time discretizations for the macroscopic system can be achieved in a similar manner by extending the definitions (3.9)–(3.11) to internal stages of the DIRK methods. At each stage, the intermediate solution $f^{(k),\star}$ is computed using the adaptive-rank method with greedy sampling, as described in Section 3.2, where the same sampling and truncation strategy is applied independently at each stage.

The full adaptive-rank update procedure within each DIRK stage consists of four successive low-rank truncations followed by a final macroscopic correction. The stage- k procedure is summarized as:

$$\{\mathcal{F}^n, \mathcal{F}^{(1)}, \dots, \mathcal{F}^{(k-1)}\} \xrightarrow{\mathcal{S}_{\epsilon_c}} \tilde{\mathcal{F}}_{\{\#,k_1\}}^{(k)} \xrightarrow{\mathcal{T}_{\epsilon_s}} \tilde{\mathcal{F}}_{\{\#,k_1 \rightarrow r_1\}}^{(k)} \xrightarrow{\mathcal{L}_{\epsilon_c}} \mathcal{F}_{\{\#,k_2\}}^{(k),\star} \xrightarrow{\mathcal{T}_{\epsilon_s}} \mathcal{F}_{\{\#,k_2 \rightarrow r_2\}}^{(k),\star} \xrightarrow{\text{LoMaC}} \mathcal{F}^{(k)}.$$

Here, $\{\mathcal{F}^n, \mathcal{F}^{(1)}, \dots, \mathcal{F}^{(k-1)}\}$ denotes the set of available low-rank numerical solutions from previous stages. Only the final corrected solution $\mathcal{F}^{(k)}$ is passed to the next stage.

For the LoMaC correction, the conservative kinetic solution at each stage is defined by

$$\mathcal{F}^{(k)} = \mathcal{F}^{(k),\star} - \mathcal{M}_{\mathbf{U}(\mathcal{F}^{(k),\star})} + \mathcal{M}_{\mathbf{U}^{(k)}}, \quad \text{for } k = 1, \dots, s, \quad (3.23)$$

where the macroscopic solution $\mathbf{U}^{(k)}$ at the internal stages is calculated according to

$$\mathbf{U}^{(k)} = \mathbf{U}^n - \Delta t \sum_{\ell=1}^k a_{k,\ell} \mathbf{F}(\mathbf{U}^{(\ell)})_x, \quad \text{for } k = 1, \dots, s, \quad (3.24)$$

and the macroscopic fluxes at the stages are defined as

$$\mathbf{F}(\mathbf{U}^{(k)}) := \left\langle \mathcal{F}^{(k)} \begin{pmatrix} v \\ v^2 \\ \frac{1}{2}v^3 \end{pmatrix} \right\rangle_v, \quad \text{for } k = 1, \dots, s. \quad (3.25)$$

We also note that there are some structural differences in the nonlinear system that arise when using DIRK methods. In the case of the fully discrete BE discretization, we need to solve a nonlinear problem (3.16) at the new time level. Correspondingly, for the high-order DIRK methods, we need to solve a sequence of nonlinear problems at each stage of the method, which we denote as

$$\mathbf{G}^{(k)}(\mathbf{U}^{(k)}) = 0, \quad \text{for } k = 1, \dots, s.$$

Here $\mathbf{G}^{(k)}$ is used to indicate that a distinct nonlinear system must be solved at each DIRK stage. These problems can be solved using the same methods discussed in Section 3.3.2.

3.5 Asymptotic Analysis

In this section, we analyze the properties of the proposed adaptive-rank method in the fluid limit. First, we recall key asymptotic properties of the full-grid high-order local SL method, as established in our previous work [10], which serves as the starting point for this study. We then show that the adaptive closure technique, used to preserve the conservation laws, also preserves the asymptotic properties of the high-order local SL method in the full-grid setting. We also analyze the impact of low-rank approximation on the asymptotic behavior. By utilizing error estimates for low-rank matrix approximations, we derive corresponding estimates that establish a relationship between the Knudsen number ϵ and the truncation errors of the CUR and SVD approximations. The local Maxwellian which characterizes the fluid limit can not be represented in terms of separable functions, except in limited circumstances. From these results, a conditional AP property of the low-rank scheme is established, and we suggest an alternative which removes these restrictions.

We first recall the AA property of the temporal discretization used in the local SL solver. As in [10] (see Theorems 3.5 and 3.6 therein), we analyze the scheme under the assumption of exact spatial discretization. Specifically, we assume that the phase space mesh has a tensor-product structure and that there is no spatial interpolation error in the reconstruction at the feet of the characteristics. The AA property holds under the additional assumption that the initial data is well-prepared, which we define as follows.

Definition 3.1. Let $\epsilon > 0$ denote a small parameter. The initial data f_0^ϵ are said to be well-prepared if they admit the formal asymptotic expansion

$$f_0^\epsilon = f_0 + \epsilon f_1 + \epsilon^2 f_2 + \dots$$

where each f_j is consistent with the order of the corresponding term in the expansion. The assumption of well-prepared initial data prevents the formation of spurious initial layers or fast transients in the limit $\epsilon \rightarrow 0$ that would otherwise need to be resolved by the discretization.

Next, we formally state the AA property of the temporal discretization for the full-grid kinetic scheme, which is as follows.

Theorem 3.2. *Suppose that the initial data are well-prepared. Consider the kinetic SL scheme defined in (3.21), using an s -stage SA DIRK method, and assume that exact spatial interpolation is used at the feet of the characteristics. Then, in the limit $\epsilon \rightarrow 0$, the temporal accuracy of the kinetic scheme implies the corresponding temporal accuracy of the macroscopic scheme defined by (3.24) and (3.25), provided that the Butcher tableau satisfies the following order conditions (valid up to third order):*

$$\begin{aligned} \text{First-order: } c_s &= 1, \\ \text{Second-order: } d_s &= \frac{1}{2}, \\ \text{Third-order: } g_s &= h_s = \frac{1}{6}, \quad G_s = \frac{1}{6}, \end{aligned}$$

where the coefficients c_s , d_s , g_s , h_s , and G_s are defined recursively according to equations (3.10) and (3.24) in [10].

A unique component of this work is its use of the macroscopic system to provide a self-consistent correction to the moments of the kinetic solution. This process enables the simultaneous preservation of mass, momentum, and energy up to a user-specified nonlinear tolerance. As discussed in Section 3.3, the high-order local SL method provides a high-quality initial guess, and a “small” correction is applied to preserve the moments. The next result shows that this process preserves the asymptotic properties of the high-order local SL method in the full-grid setting.

Theorem 3.3. *Suppose the initial data are well-prepared, and assume that the fully-discrete kinetic scheme is AP but does not simultaneously preserve mass, momentum, and energy. Then, the self-consistent macroscopic correction procedure defined in (3.24) and (3.25), when applied to the intermediate solutions $f^{(k)}$ from (3.23), preserves the underlying AP property of the scheme. Moreover, if the full-discrete kinetic scheme is also AA, then the macroscopic correction preserves the AA property as well.*

Proof. Suppose that the fully-discrete scheme is AP. Then, by definition, it follows that the discrete kinetic solution satisfies

$$F^{(k),\star} = \mathcal{M}_{\mathbf{U}(F^{(k),\star})} + \mathcal{O}(\epsilon), \quad \text{for } k = 1, \dots, s. \quad (3.26)$$

Here, we use $F^{(k),\star}$ to distinguish the non-conservative kinetic solution from its fully-conservative (mass, momentum, and energy) counterpart.

Now consider the self-consistent macroscopic stage values $\mathbf{U}^{(k)}$ defined by the moment equations (3.24) and (3.25). These are closed using the corrected kinetic distribution $F^{(k)}$, which is constructed following the conservative format (3.23) and is given by

$$F^{(k)}(\mathbf{U}^{(k)}) = F^{(k),\star} - \mathcal{M}_{\mathbf{U}(F^{(k),\star})} + \mathcal{M}_{\mathbf{U}(F^{(k)})}.$$

Substituting (3.26) into this expression and taking the limit $\epsilon \rightarrow 0$, we obtain

$$F^{(k)}(\mathbf{U}^{(k)}) = \mathcal{M}_{\mathbf{U}^{(k)}}, \quad \text{for } k = 1, \dots, s.$$

This limiting solution provides the necessary closure to the macroscopic flux defined by (3.25), namely

$$\mathbf{F}(\mathbf{U}^{(k)}) := \left\langle \mathcal{M}_{\mathbf{U}^{(k)}} \begin{pmatrix} v \\ v^2 \\ \frac{1}{2}v^3 \end{pmatrix} \right\rangle_v, \quad \text{for } k = 1, \dots, s.$$

When combined with the self-consistent discretization of the system (3.24), we obtain the compressible Euler equations. Therefore, the correction process preserves the AP property of the kinetic scheme. If the fully-discrete kinetic scheme is also AA, then the discretization of the self-consistent macroscopic system converges at the same order of accuracy as the kinetic scheme, since the same DIRK method is employed for both systems. Furthermore, the deviations from the local Maxwellian are again $\mathcal{O}(\epsilon)$, so this property remains unaffected. \square

In the low-rank setting, the use of low-rank approximations may cause the solution to deviate from the correct asymptotic limit. Each of the approximations contributes to the overall truncation error, which we now quantify in the following result.

Theorem 3.4. *Suppose that a SA DIRK temporal discretization with the AA property, satisfying the conditions of Theorem 3.2, is paired together with a local SL solver. Then, at the end of each stage k , the conservative low-rank solution $\mathcal{F}^{(k)}$ defined following (3.23), satisfies the following truncation error bound*

$$\left\| \mathcal{F}^{(k)} - \mathcal{M}_{\mathbf{U}(\mathcal{F}^{(k)})} \right\| \lesssim \epsilon + \left\| E_{\epsilon_s}(\mathcal{F}_{\{\#,k_2\}}^{(k)}) \right\| + \left\| E_{\epsilon_c}(F^{(k)}) \right\|,$$

where we denote the truncation errors due to the CUR and SVD approximations as

$$E_{\epsilon_s}(\mathcal{F}_{\{\#,k_2\}}^{(k)}) := \mathcal{F}_{\{\#,k_2 \rightarrow r_2\}}^{(k)} - \mathcal{F}_{\{\#,k_2\}}^{(k)}, \quad E_{\epsilon_c}(F^{(k)}) := \mathcal{F}_{\{\#,k_2\}}^{(k)} - F^{(k)}.$$

Proof. Using the definition of the conservative form of the low-rank solution (3.23), we can decompose the error as

$$\begin{aligned} \mathcal{F}^{(k)} - \mathcal{M}_{\mathbf{U}(\mathcal{F}^{(k)})} &= \mathcal{F}_{\{\#,k_2 \rightarrow r_2\}}^{(k),\star} - \mathcal{M}_{\mathbf{U}(\mathcal{F}_{\{\#,k_2 \rightarrow r_2\}}^{(k),\star})}, \\ &= F^{(k)} - \mathcal{M}_{\mathbf{U}(F^{(k)})} + \mathcal{F}_{\{\#,k_2 \rightarrow r_2\}}^{(k),\star} - F^{(k)} + \mathcal{M}_{\mathbf{U}(F^{(k)})} - \mathcal{M}_{\mathbf{U}(\mathcal{F}_{\{\#,k_2 \rightarrow r_2\}}^{(k),\star})}. \end{aligned} \quad (3.27)$$

Since the initial data is well-prepared and the local solver is AA, then we immediately have that

$$\left\| F^{(k)} - \mathcal{M}_{\mathbf{U}(F^{(k)})} \right\| \lesssim \epsilon. \quad (3.28)$$

The second term can be estimated by further decomposing the error into the two parts. One concerns the SVD truncation of a CUR object, while the other represents the approximation error for the CUR decomposition of full-rank data. This gives

$$\mathcal{F}_{\{\#,k_2 \rightarrow r_2\}}^{(k),\star} - F^{(k)} = \mathcal{F}_{\{\#,k_2 \rightarrow r_2\}}^{(k),\star} - \mathcal{F}_{\{\#,k_2\}}^{(k),\star} + \mathcal{F}_{\{\#,k_2\}}^{(k),\star} - F^{(k)} := E_{\epsilon_s}(\mathcal{F}_{\{\#,k_2\}}^{(k),\star}) + E_{\epsilon_c}(F^{(k)}). \quad (3.29)$$

The last term involves a difference between two Maxwellians, which can be estimated using the Mean Value Theorem and the error equation (3.29), together with the triangle inequality. That is, there exists an $\mathcal{F}_*^{(k)}$ such that

$$\left\| \mathcal{M}_{\mathbf{U}(F^{(k)})} - \mathcal{M}_{\mathbf{U}(\mathcal{F}_{\{\#,k_2 \rightarrow r_2\}}^{(k)})} \right\| \leq \left\| \mathcal{M}'_{\mathbf{U}(\mathcal{F}_*^{(k)})} \right\| \left(\left\| E_{\epsilon_s}(\mathcal{F}_{\{\#,k_2\}}^{(k),*}) \right\| + \left\| E_{\epsilon_c}(F^{(k)}) \right\| \right). \quad (3.30)$$

In the above, $\mathcal{M}'_{\mathbf{U}(\mathcal{F}_*^{(k)})}$ denotes the Jacobian matrix of a local Maxwellian, which will be bounded provided that the moments of $\mathcal{F}_*^{(k)}$ satisfy $\rho_*^{(k)} \geq \rho_m > 0$ and $T_*^{(k)} \geq T_m > 0$.

Finally, applying the triangle inequality to (3.27) together with each of the inequalities in (3.28) to (3.30), we obtain the result provided in the statement. This completes the proof. \square

The term $E_{\epsilon_s}(\mathcal{F}_{\{\#,k_2\}}^{(k),*})$ in (3.29) requires some additional explanation. Recall (3.22), which provides the following element-wise definition to build the CUR decomposition $\mathcal{F}_{\{\#,k_2\}}^{(k),*}$. In the limit $\epsilon \rightarrow 0$, this formula reduces to

$$(\mathcal{F}_{\{\#,k_2\}}^{(k),*})_{i,j} = \left(\mathcal{M}_{\mathbf{U}(\tilde{\mathcal{F}}_{\{\#,k_1 \rightarrow r_1\}}^{(k)})} \right)_{i,j}.$$

As $\tilde{\mathcal{F}}_{\{\#,k_1 \rightarrow r_1\}}^{(k)}$ is constructed using both CUR and SVD approximations, there will be an accumulation of the truncation errors due to earlier stages, resulting in a perturbed local Maxwellian that will be approximated by a CUR decomposition. Due to the interpolation property of the CUR decomposition, the previous limiting equality will be enforced only at selected indices and will be approximate elsewhere. To analyze the truncation error at the interpolation points, let

$$\tilde{\mathcal{F}}_{\{\#,k_1 \rightarrow r_1\}}^{(k)} = \tilde{\mathcal{F}}_{\{\#,k_1 \rightarrow r_1\}}^{(k)} - \tilde{\mathcal{F}}_{\{\#,k_1\}}^{(k)} + \tilde{\mathcal{F}}_{\{\#,k_1\}}^{(k)} - \tilde{F}^{(k)} + \tilde{F}^{(k)} := E_{\epsilon_s}(\tilde{\mathcal{F}}_{\{\#,k_1\}}^{(k)}) + E_{\epsilon_c}(\tilde{F}^{(k)}) + \tilde{F}^{(k)}.$$

Again, by the Mean Value Theorem, there exists (another) $\mathcal{F}_*^{(k)}$ such that

$$(\mathcal{F}_{\{\#,k_2\}}^{(k),*})_{i,j} = \left(\mathcal{M}_{\mathbf{U}(\tilde{F}^{(k)})} \right)_{i,j} + \left(\mathcal{M}'_{\mathbf{U}(\mathcal{F}_*^{(k)})} \left[E_{\epsilon_s}(\tilde{\mathcal{F}}_{\{\#,k_1\}}^{(k)}) + E_{\epsilon_c}(\tilde{F}^{(k)}) \right] \right)_{i,j}. \quad (3.31)$$

Although this equality holds only at select interpolation points, it illustrates the accumulation of truncation error from the earlier stages of the method. As the subsequent SVD truncation destroys the interpolation property of CUR, it is difficult to say more about this accumulation of error.

We now state the main limiting property of the proposed method which appears as a corollary of Theorem 3.4. More specifically, we establish a *conditional* AA property, which is analytically satisfied if the limiting solution exhibits rank degeneracy.

Corollary 3.5. Let an s -stage SA DIRK method with the AA property (satisfying the conditions of Theorem 3.2) be coupled with a local SL solver and the macroscopic correction procedure defined by (3.23) to (3.25). Then the proposed low-rank scheme satisfies the AA property in the limit $\epsilon \rightarrow 0$, provided that for each stage $k = 1, \dots, s$, the following condition holds:

$$\left\| E_{\epsilon_s}(\mathcal{F}_{\{\#,k_2\}}^{(k)}) \right\| + \left\| E_{\epsilon_c}(F^{(k)}) \right\| \lesssim \epsilon.$$

Remark 3.6. To preserve the AA property of the full-grid scheme, the low-rank truncation errors must not perturb the distribution significantly away from the local Maxwellian. This condition

is automatically satisfied for *any* distribution if the truncation tolerances ϵ_c and ϵ_s are chosen to be $\mathcal{O}(\epsilon)$. However, doing so may undermine the efficiency of the low-rank method, as it may require large ranks to achieve such high accuracy. The key advantage of the proposed scheme is recovered when the limiting solution exhibits *rank degeneracy* when $\epsilon \rightarrow 0$ — that is, when the local Maxwellian can be exactly written using separable functions. In this setting, it is possible to choose tolerances of size $\mathcal{O}(\epsilon)$ while maintaining a low computational cost.

Remark 3.7. To alleviate the restriction on the truncation tolerances in Corollary 3.5, one could alternatively consider a *multiplicative* decomposition of the distribution function, i.e., $f = \mathcal{M}_{\mathbf{U}(f)}g$, and apply the low-rank decomposition only to the function g , which is a rank-1 function when $\epsilon \rightarrow 0$. This idea has been considered in other low-rank methods [2, 12] for the case of isothermal Maxwellians with and without drift. The use of a multiplicative decomposition requires additional modifications to the scheme presented in this work, so we do not consider this approach here and leave it to future work.

4 Numerical Tests

In this section, we evaluate the proposed low-rank method using benchmark problems for the BGK model. We study the accuracy of the method across a range of ϵ . Additionally, we demonstrate the capability of the method to capture shocks and discontinuous solution structures by applying them to a classical Riemann problem. To demonstrate the capabilities of the method in addressing multi-scale problems, we also consider a more challenging mixed regime problem.

In all experiments, we use a four-stage third-order DIRK method, which is asymptotically accurate for the BGK model, and the interval $[-10, 10]$ is used for the velocity domain. Note that the Butcher table for the scheme can be found in Table B10 of [10]). With regard to the JFNK method, we used a tolerance of 10^{-14} for the Newton method and a tolerance of 10^{-6} for the inner Krylov solver. The time step in the simulations is calculated from the CFL as $\Delta t = \text{CFL} \Delta x / |v_{\max}|$. In certain examples, we measure the absolute error in a conserved quantity $q(x, t)$, e.g., mass, momentum, and energy, as $|Q(t) - Q(0)|$, where we have defined

$$Q(t) = \int_{\Omega_x} q(x, t) dx \approx \Delta x \sum_{i=1}^{N_x} q_i(t).$$

Example 4.1. (Consistent initial data [27]) Consider the BGK model with the initial Maxwellian distribution:

$$f(x, v, 0) = \frac{\rho_0}{\sqrt{2\pi T_0}} \exp\left(-\frac{(v - u_0)^2}{2T_0}\right), \quad x \in [-1, 1] \quad (4.1)$$

with initial density $\rho_0(x) = 1$, initial temperature $T_0(x) = 1$, and initial mean velocity:

$$u_0(x) = \frac{1}{10} [\exp(-(10x - 1)^2) - 2 \exp(-(10x + 3)^2)].$$

We apply periodic boundary conditions and set the final time to $t = 0.04$. The relative truncation tolerances for the CUR and SVD approximations are set to $\epsilon_c = 10^{-9}$ and $\epsilon_s = 10^{-8}$, respectively.

In Figure 4.4, we present the results of a temporal refinement study for various values of ϵ . We use a fixed mesh with size 128×128 for this study, and compare the solutions against a reference solution obtained using the same mesh and a CFL number of 0.001. The methods exhibit third-order accuracy in time, with convergence saturation occurring at smaller CFL numbers, where the spatial error becomes dominant. During this study, we also recorded the average CUR and SVD

ranks for each case. As shown in Figure 4.5, the average solution rank remains largely unchanged across the different CFL numbers. However, we observe that smaller values of ϵ tend to yield smaller average ranks, as the system transitions to equilibrium more quickly. The average number of Newton and Krylov iterations at each stage of the time integration are plotted as functions of the CFL in Figure 4.6. The results indicate that smaller values of ϵ generally require slightly more iterations, but the increase is not substantial. However, as the CFL number increases, the number of nonlinear and linear iterations tends to rise. For moderate CFL numbers (e.g., CFL < 10), the iteration counts remain small, so preconditioning for the inner Krylov method may not be necessary. For larger CFL numbers, preconditioning will be essential to ensure the robustness of the solver. This aspect of the methods will be explored in future work.

In Table 4.1, we summarize the results from a spatial refinement study, where the mesh resolution is successively doubled from $N_x = 16$ to $N_x = 128$, using a fixed CFL number of 4. Third-order accuracy is observed using the L^1 error in both the kinetic and fluid limits, which is consistent with the third-order DIRK scheme employed in the proposed method. We remark that achieving fifth order accuracy requires the use of a smaller CFL number as well as a smaller values for the truncation tolerances, which will increase the storage cost of the method. The conservative property of the method is verified by measuring the absolute errors in mass, momentum, and energy, with all quantities being conserved to machine precision. Moreover, the average solution rank and iteration numbers for the nonlinear and linear problems remain small throughout the simulation.

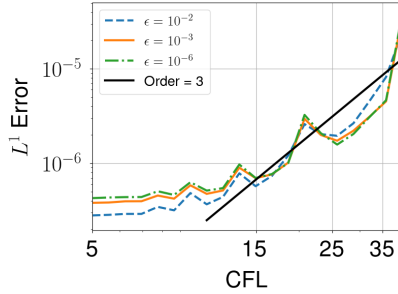


Figure 4.4: (Consistent initial data) Convergence results for a temporal refinement study.

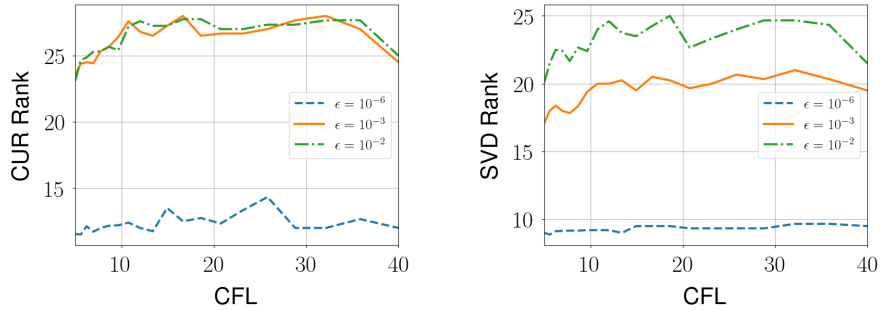


Figure 4.5: (Consistent initial data). CUR (left) and SVD (right) rank versus CFL for different ϵ .

Example 4.2. (Riemann problem [31]) Next, we investigate the capabilities of the proposed methods in capturing smooth rarefaction waves as well as non-smooth solution structures, including contact discontinuities and shocks, found in compressible gas dynamics problems. Consider the

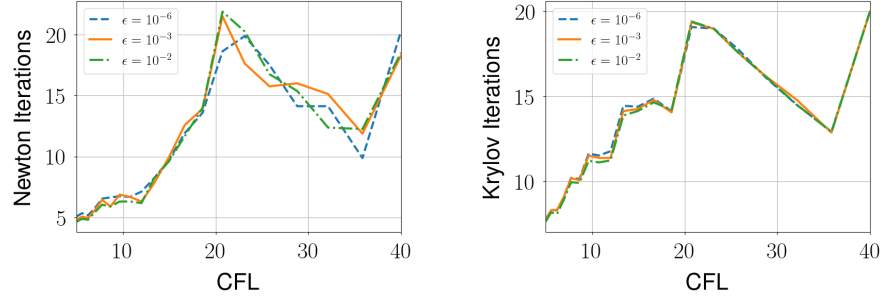


Figure 4.6: (Consistent initial data). Average number of Newton (left) and Krylov (right) iterations per stage as a function of the CFL for different ϵ .

Table 4.1: (Consistent initial data). Spatial refinement results using different values of ϵ .

ϵ	N_x	L^1 error	Order	ρ	ρu	E	SVD	CUR	Newton	Krylov
10^{-2}	16	3.0e-04	—	2e-16	3e-18	2e-16	6.0	7.0	4.4	5.5
	32	4.2e-05	2.84	4e-16	0e+00	0e+00	9.5	11.2	3.8	6.1
	64	4.8e-06	3.14	4e-16	3e-18	2e-16	15.2	18.0	3.5	6.9
	128	2.8e-07	4.10	4e-16	0e+00	2e-16	20.4	22.8	4.1	6.8
10^{-3}	16	6.6e-04	—	2e-16	3e-18	0e+00	5.7	7.0	4.6	5.5
	32	4.9e-05	3.73	4e-16	3e-18	0e+00	9.2	11.0	4.6	5.5
	64	5.7e-06	3.11	4e-16	3e-18	2e-16	14.5	18.3	3.9	7.1
	128	3.8e-07	3.92	4e-16	3e-18	2e-16	16.6	22.5	4.4	6.9
10^{-6}	16	9.1e-04	—	2e-16	3e-18	0e+00	5.7	7.0	5.0	5.3
	32	5.1e-05	4.15	4e-16	0e+00	2e-16	8.0	10.2	3.7	6.2
	64	6.3e-06	3.03	4e-16	0e+00	0e+00	8.7	12.3	4.0	7.2
	128	4.2e-07	3.88	4e-16	0e+00	2e-16	8.9	11.6	4.8	6.9

following initial distribution, which exhibits discontinuous behavior:

$$f(x, v, 0) = \begin{cases} \frac{\rho_L}{\sqrt{2\pi T_L}} \exp\left(-\frac{(v - u_L)^2}{2T_L}\right) & x \in [0, 0.5], \\ \frac{\rho_R}{\sqrt{2\pi T_R}} \exp\left(-\frac{(v - u_R)^2}{2T_R}\right) & x \in [0.5, 1], \end{cases} \quad (4.2)$$

where $(\rho_L, u_L, T_L) = (2.25, 0, 1.125)$ and $(\rho_R, u_R, T_R) = (3/7, 0, 1/6)$. Fixed boundary conditions are applied, using values from the initial condition. The phase space is discretized with a mesh containing 256×256 cells in space and velocity, respectively. The simulation runs until a final time of $t = 0.16$, with a CFL number of 4. The relative truncation tolerances for the CUR and SVD approximations are set to $\varepsilon_c = 10^{-4}$ and $\varepsilon_s = 10^{-3}$.

The macroscopic density, velocity, and temperature at the final time step are presented in Figure 4.7. The lines in each plot correspond to different Knudsen numbers, specifically $\epsilon = 10^{-6}$, $\epsilon = 10^{-3}$, and $\epsilon = 10^{-2}$. Our results align well with those from [27], with sharper solution features emerging as ϵ decreases. These non-smooth features are consistent with the behavior expected from the compressible Euler system.

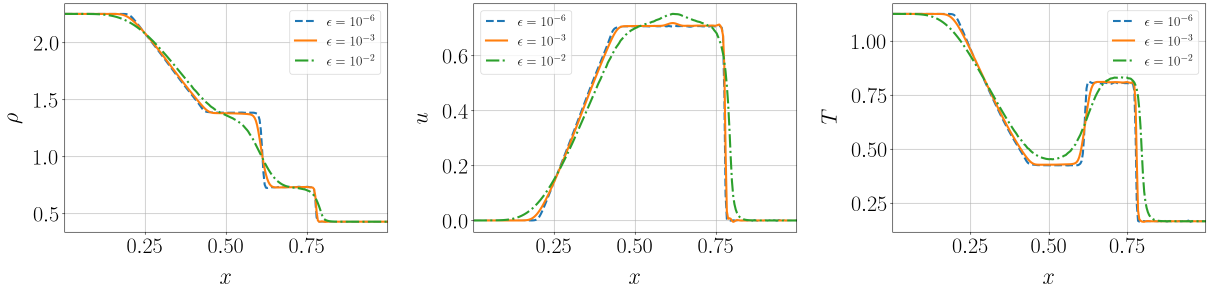


Figure 4.7: (Riemann problem). The macroscopic quantities ρ (left), u (middle), and T (right) at time $t = 0.16$ using different values of ϵ .

Figure 4.8 presents the SVD and CUR rank data as functions of time. As ϵ decreases, the rank of the solution decreases as well, with this effect being more pronounced in the SVD data. For $\epsilon = 10^{-2}$, the SVD and CUR ranks initially increase at earlier times before reaching a plateau. This increase likely corresponds to the rapid evolution of solution features that occur shortly after the interaction of the Riemann states.

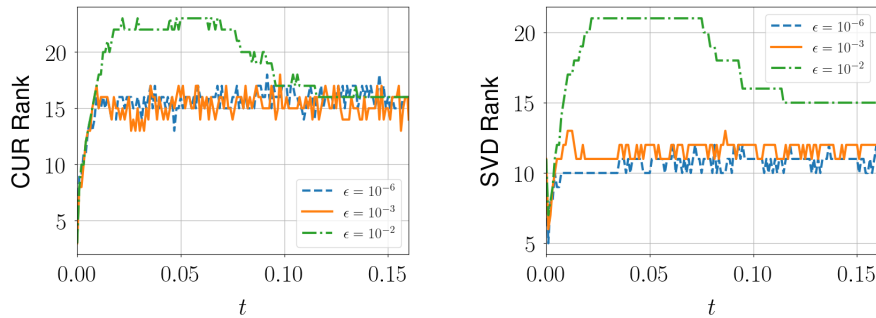


Figure 4.8: (Riemann problem). CUR (left) and SVD (right) solution rank versus time for different values of ϵ .

The average number of Newton and Krylov iterations at each stage of the time integration is shown as a function of time in Figure 4.9. Our results indicate that smaller values of ϵ generally lead to a slightly higher number of iterations, but the increase is not substantial. Again, the iteration counts remain small across all cases, even though no preconditioning strategy is applied to the inner Krylov method.

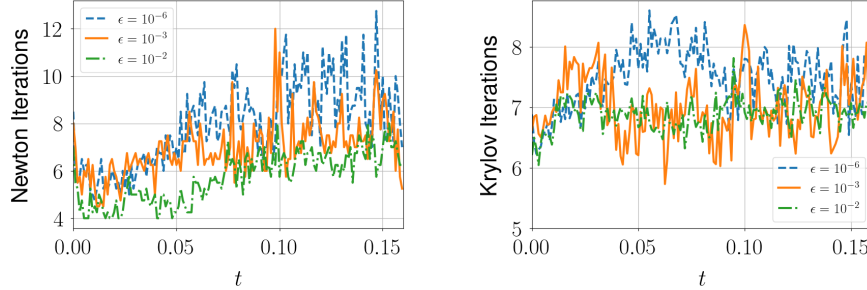


Figure 4.9: (Riemann problem). Average number of Newton (left) and Krylov (right) iterations per stage as a function of time obtained with different values of ϵ .

Example 4.3. (Mixed regime problem [37]) We now apply the proposed method to a more challenging mixed-regime problem to evaluate its ability to handle multi-scale features. We consider a spatially dependent Knudsen number, denoted as $\epsilon(x)$, defined as

$$\epsilon(x) = \epsilon_0 + \frac{1}{2} \left(\tanh(1 - a_0 x) + \tanh(1 + a_0 x) \right), \quad (4.3)$$

where $\epsilon_0 = 10^{-6}$ and a_0 is a scalar parameter that effectively tunes the width of $\epsilon(x)$. We explore two specific configurations where the transitions between the fluid and kinetic limits are either slow ($a_0 = 11$) or fast ($a_0 = 40$). A plot of the Knudsen number defined by (4.3) is shown in Figure 4.10 with these two values of a_0 . The limiting regimes are separated by approximately six orders of magnitude, and include a full range of intermediate regimes. While methods can be developed to treat the distinct limits in this problem, the proposed method offers a simplified approach to simultaneously address each of the limits, including the intermediate regimes.

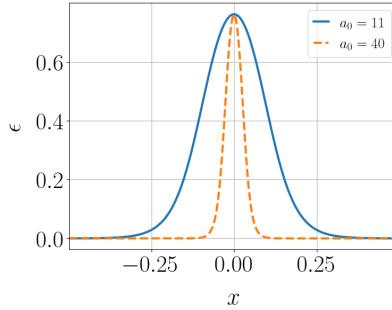


Figure 4.10: (Mixed regime problem). The Knudsen number $\epsilon(x)$ obtained with $a_0 = 11$ and $a_0 = 40$.

The consistent initial distribution for this problem is given by

$$f(x, v, 0) = \frac{\rho_0}{2\sqrt{2\pi T_0}} \left[\exp\left(-\frac{(v - u_0)^2}{2T_0}\right) + \exp\left(-\frac{(v + u_0)^2}{2T_0}\right) \right], \quad x \in [-0.5, 0.5],$$

where

$$\rho_0(x) = 1 + 0.875 \sin(2\pi x), \quad u_0(x) = 0.75, \quad T_0(x) = 0.5 + 0.4 \sin(2\pi x).$$

We apply periodic boundary conditions and discretize phase space using a 256×256 mesh. The final simulation time is $t = 0.45$, and each configuration is considered for three different CFL numbers: 1, 1.5, and 2. We use $\varepsilon_c = 10^{-8}$ and $\varepsilon_s = 10^{-7}$ as the relative truncation tolerances for the CUR and SVD approximations.

Plots of the macroscopic variables ρ , u , and T , at $t = 0.1$, $t = 0.3$, and $t = 0.45$, using $a_0 = 11$ and $a_0 = 40$, are shown in Figure 4.11 and Figure 4.12, respectively, using different CFL numbers. In general, for $a_0 = 11$, the solution exhibits simple, localized structures with some non-smooth features, such as jumps and kinks. In contrast, for $a_0 = 40$, the rapid transition between fluid and kinetic regimes leads to more complex dynamics, in particular, larger jumps and discontinuities. Interestingly, the results across different CFL numbers are visually indistinguishable, even at later times, despite the larger time steps in simulations with higher CFL numbers.

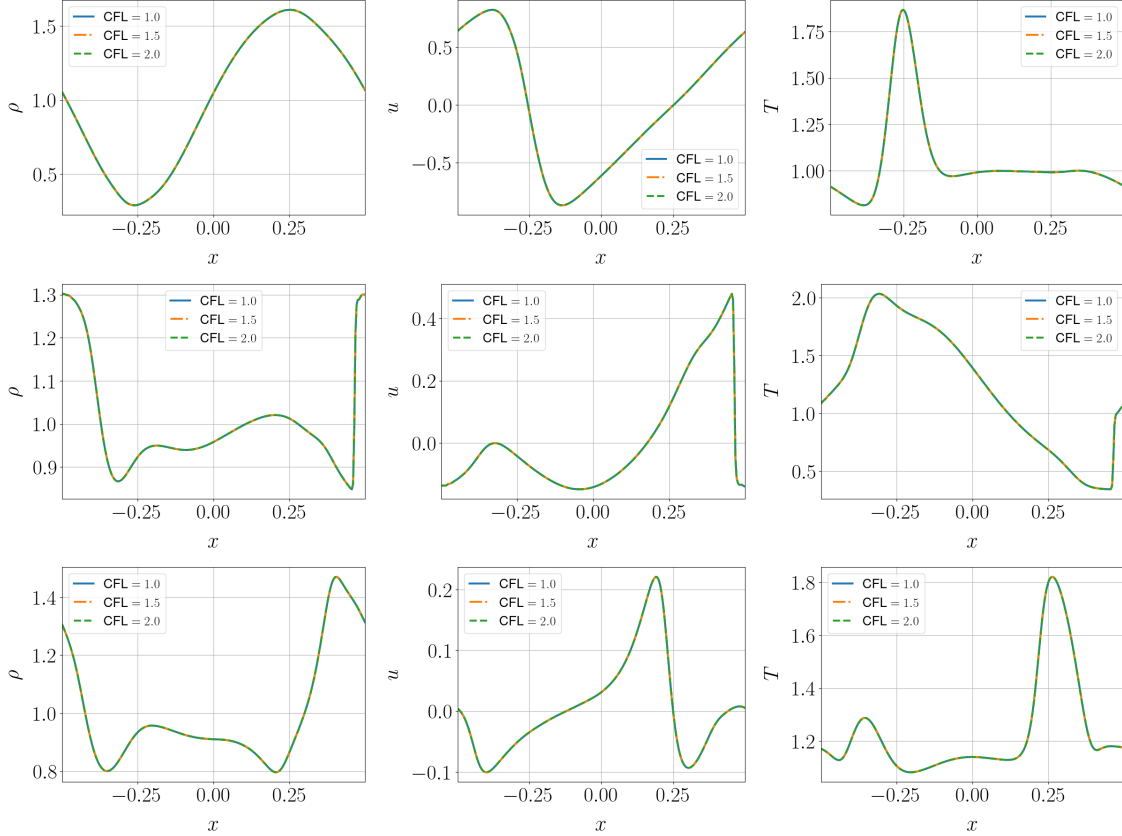


Figure 4.11: (Mixed regime problem, $a_0 = 11$). The macroscopic quantities ρ , u , and T are shown at time $t = 0.1$ (top row), $t = 0.3$ (middle row), $t = 0.45$ (bottom row) with different CFL numbers.

The CUR and SVD ranks for both configurations are presented in Figure 4.13 as a function of time. As expected, the CUR rank is slightly larger than the SVD rank, but both ranks are comparable across the range of CFL values considered. For the case $a_0 = 11$, the solution structures are relatively simple, resulting in small SVD and CUR ranks over time. From this data, we find that the low-rank approach requires approximately 15% of the storage compared to the full grid method. In contrast, larger ranks are observed for $a_0 = 40$, where more abrupt transitions occur

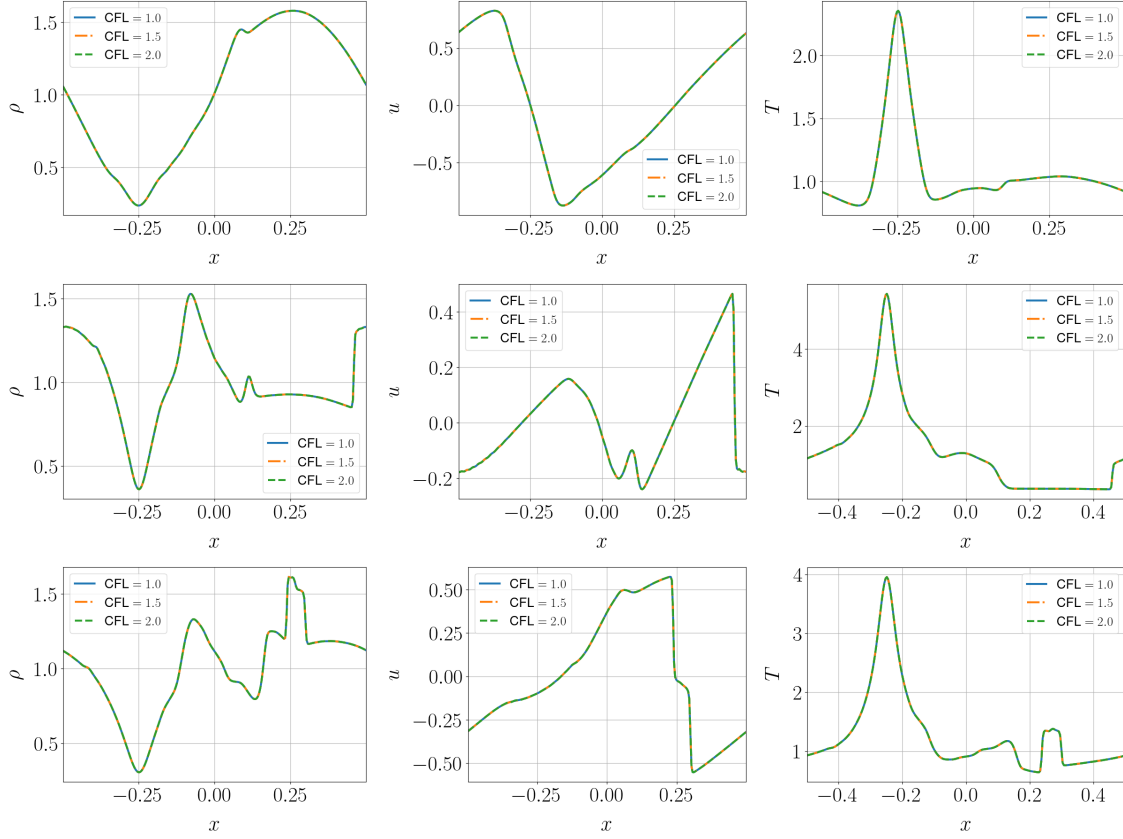


Figure 4.12: (Mixed regime problem, $a_0 = 40$). The macroscopic quantities ρ , u , and T are shown at time $t = 0.1$ (top row), $t = 0.3$ (middle row), $t = 0.45$ (bottom row) with different CFL numbers.

between the fluid and kinetic regimes. Here, the low-rank approach uses approximately 23% of the storage required by the full grid method, which is higher than the case for $a_0 = 11$. This behavior is expected due to the presence of discontinuities in the solution, as shown in Figure 4.12.

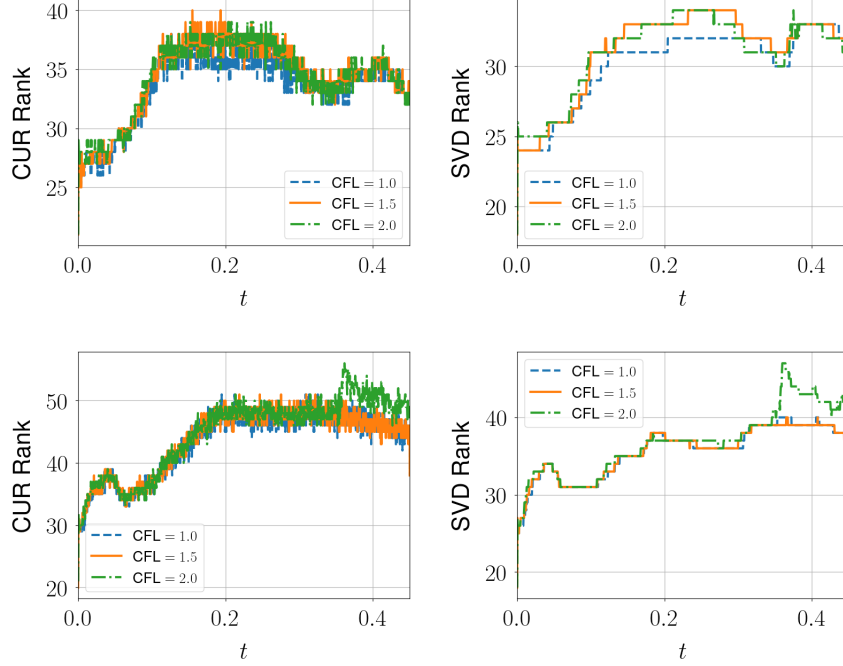


Figure 4.13: (Mixed regime problem). CUR and SVD rank over time using different CFL numbers. Figures in the top and bottom rows correspond to $a_0 = 11$ and $a_0 = 40$, respectively.

Figure 4.14 displays the average number of Newton and Krylov iterations per stage as a function of time. Again, we observe that the number of iterations remains small throughout the simulation, so we find preconditioning to not be necessary. This is primarily due to the high-quality initial guess provided by the low-rank kinetic solver, which significantly improves the convergence of the nonlinear solver. The number of iterations in both cases of a_0 are generally similar. However, the number of iterations generally increases with the CFL number, as observed in Figure 4.6. In each configuration, the method conserves total mass, momentum, and energy to machine precision, as demonstrated in Figure 4.15.

Lastly, Figure 4.16 presents a plot of the simulation wall time per step versus N , the number of mesh points per dimension. A shorter final time of $T = 0.001$ was used with $\text{CFL} = 1$, and the value of N was successively doubles from $N = 8$ to $N = 2048$. In both cases, i.e., $a_0 = 11$ and $a_0 = 40$, we observe the correct linear scaling with respect to the mesh size N in the proposed adaptive-rank method.

5 Conclusion

In this work, we introduced a novel adaptive-rank method for the BGK equations that simultaneously achieves mass, momentum, and energy conservation and possesses a conditionally AP property. This method builds on our previous work by extending the greedy ACA with SVD truncation to address stiff collision operators. The greedy ACA plays a crucial role in the method and serves two key purposes: (1) It identifies the points on the mesh that are to be updated using a local

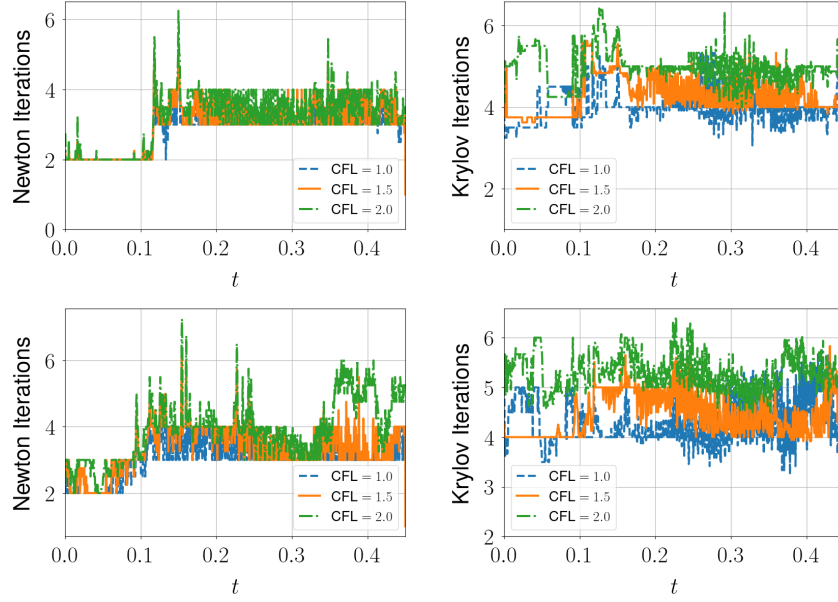


Figure 4.14: (Mixed regime problem). Average number of iterations per stage over time obtained with different CFL numbers. The top and bottom rows represent $a_0 = 11$ and $a_0 = 40$, respectively.

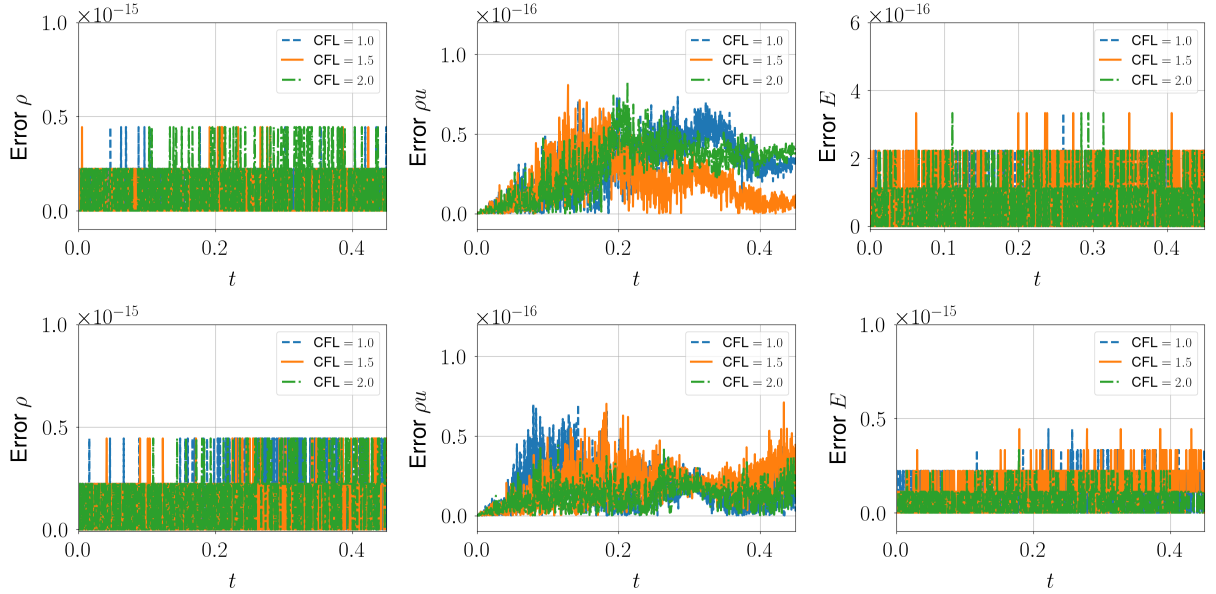


Figure 4.15: (Mixed regime problem). Absolute error in conserved quantities as a function of time. The top and bottom rows correspond to $a_0 = 11$ and $a_0 = 40$, respectively.

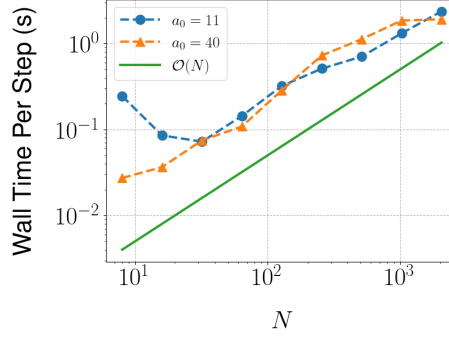


Figure 4.16: (Mixed regime problem). Simulation wall time per step versus the number of mesh points per dimension using a fixed CFL with $a_0 = 11$ and $a_0 = 40$.

SL solver and (2) enables a point-wise evaluation of the local Maxwellian in the BGK operator. The latter is particularly beneficial because local Maxwellians generally do not admit a low-rank decomposition, making this feature a distinctive advantage of our approach. In future work, we shall consider a multiplicative decomposition of the distribution function, which will expose more low-rank structure in the kinetic problem. We expect that the theorems developed in this work will be largely strengthened by such considerations, as the limiting solution has provable low-rank structure.

We also proposed a robust technique for strictly enforcing conservation laws within the kinetic solution. This technique iteratively corrects the moments of the low-rank solution using a high-order solution of the conserved macroscopic system, which is closed in a dynamic and self-consistent manner. The iterative solver for this macroscopic system is based on a highly efficient Newton-Krylov method, which allows for an entirely matrix-free implementation. Despite the fact that the provisional low-rank solution is non-conservative, it serves as a high-quality initial guess for the implicit macroscopic solver. Even for modest CFL numbers, we find that the overhead of this iteration is not significant, even when preconditioning is not applied.

To achieve high-order accuracy, we combined WENO spatial reconstructions with third-order DIRK methods that are stiffly accurate. The accuracy and efficacy of the proposed method was established using standard benchmark problems, including those with smooth and non-smooth solution structures, across a broad range of ϵ . The proposed method is capable of capturing a wide range of phenomena that spans both fluid and kinetic regimes. In the final experiment, the method was applied to a challenging mixed regime problem in which the size of the Knudsen number varies by roughly six orders in magnitude. This example also highlights the advantage of the SL method, which permits a much larger time step to be used in simulations.

In summary, the low-rank method presented in this work offers a powerful framework for solving multi-scale kinetic equations with stiff collision operators while preserving key physical properties. The flexibility of the method, combined with its efficiency and strict conservation, provides a significant advancement in the simulation of multi-scale kinetic problems. Future work will focus on extending the method to high-dimensional problems through novel low-rank formats. We also plan to explore preconditioning techniques for the macroscopic system. While simple preconditioners such as incomplete LU factorizations could be applied, they require access to the Jacobian matrix, which increases both storage and computational cost of the method. These techniques may not be feasible for high-dimensional problems; however, other strategies, such as physics-based preconditioning [29, 24, 32, 19] may be more appropriate for large scale problems in high dimensions. The BGK equation is a natural first step in the treatment of collisional problems, but it known to be

accurate only when the system is “close” to equilibrium. Future investigations will focus on more complex collision models with non-local, nonlinear effects that may better capture the full range of kinetic behaviors.

6 Acknowledgments

This work was partially supported Department of Energy DE-SC0023164 by the Multifaceted Mathematics Integrated Capability Centers (MMICCs) program of DOE Office of Applied Scientific Computing Research (ASCR), and Air Force Office of Scientific Research (AFOSR) FA9550-241-0254 via the Multidisciplinary University Research Initiatives (MURI) Program. We also wish to acknowledge support provided by NSF grant NSF-DMS-2111253 as well as grant FA9550-22-1-0390 from the Air Force Office of Scientific Research.

Appendices

A Low-Rank Numerical Integration for Macroscopic Flux

To efficiently evaluate the numerical integrals $\widetilde{\int}_{\mathbb{R}^\pm} \cdot dv$, we consider the numerical integrals of an SVD solution $U\Sigma V^\top$ and an analytical Maxwellian $\mathcal{M}_{\mathcal{U}}$, which are the two basic components used to evaluate the flux (3.12). The flux for the SVD component can be approximated using the midpoint rule, which gives

$$\widetilde{\int}_{\mathbb{R}^\pm} f \begin{pmatrix} v \\ v^2 \\ \frac{1}{2}v^3 \end{pmatrix} dv \approx \Delta v \begin{pmatrix} U\Sigma V^\top \mathbf{v}^\pm \\ U\Sigma V^\top (\mathbf{v}^\pm)^2 \\ \frac{1}{2}U\Sigma V^\top (\mathbf{v}^\pm)^3 \end{pmatrix}, \quad (\text{A.1})$$

where the wind directions are given by

$$\mathbf{v}^+ = \max(\mathbf{v}, 0), \quad \mathbf{v}^- = \min(\mathbf{v}, 0).$$

For the Maxwellian component, we can directly use the following analytical formulas:

$$\begin{aligned} \int_{\mathbb{R}^\pm} \mathcal{M}_{\mathcal{U}} dv &= \frac{\rho}{2} \left(1 \pm \operatorname{erf} \left(\frac{u}{\sqrt{2T}} \right) \right), \\ \int_{\mathbb{R}^\pm} \mathcal{M}_{\mathcal{U}} v dv &= u \int_{\mathbb{R}^\pm} \mathcal{M}_{\mathcal{U}} dv \pm T \mathcal{M}_{\mathcal{U}}|_{v=0}, \\ \int_{\mathbb{R}^\pm} \mathcal{M}_{\mathcal{U}} v^2 dv &= 2u \int_{\mathbb{R}^\pm} \mathcal{M}_{\mathcal{U}} v dv + (T - u^2) \int_{\mathbb{R}^\pm} \mathcal{M}_{\mathcal{U}} dv \mp uT \mathcal{M}_{\mathcal{U}}|_{v=0}, \\ \int_{\mathbb{R}^\pm} \mathcal{M}_{\mathcal{U}} v^3 dv &= 3u \int_{\mathbb{R}^\pm} \mathcal{M}_{\mathcal{U}} v^2 dv - 3u^2 \int_{\mathbb{R}^\pm} \mathcal{M}_{\mathcal{U}} v dv + u^3 \int_{\mathbb{R}^\pm} \mathcal{M}_{\mathcal{U}} dv + (\mp u^2 \pm 2T^2 uT) \mathcal{M}_{\mathcal{U}}|_{v=0}, \end{aligned} \quad (\text{A.2})$$

where ρ , u , and T are the corresponding physical quantities of the Maxwellian $\mathcal{M}_{\mathcal{U}}$, and $\operatorname{erf}(\cdot)$ is the Gauss error function.

References

- [1] R. ALEXANDER, *Diagonally implicit Runge–Kutta methods for stiff ODE’s*, SIAM Journal on Numerical Analysis, 14 (1977), pp. 1006–1021.
- [2] L. BAUMANN, L. EINKEMMER, C. KLINGENBERG, AND J. KUSCH, *A stable multiplicative dynamical low-rank discretization for the linear Boltzmann-BGK equation*, arXiv preprint arXiv:2411.06844, (2024).
- [3] P. BHATNAGAR, E. GROSS, AND M. KROOK, *A model for collision processes in gases. I. small amplitude processes in charged and neutral one-component systems*, Physical review, 94 (1954), p. 511.
- [4] G. CERUTI AND C. LUBICH, *An unconventional robust integrator for dynamical low-rank approximation*, BIT Numerical Mathematics, 62 (2022), pp. 23–44.
- [5] S. CHAPMAN AND T. G. COWLING, *The mathematical theory of non-uniform gases: an account of the kinetic theory of viscosity, thermal conduction and diffusion in gases*, Cambridge university press, 1990.
- [6] A. CIVRIL AND M. MAGDON-ISMAIL, *Finding maximum volume sub-matrices of a matrix*, RPI Comp Sci Dept TR, (2007), pp. 07–08.
- [7] A. DEKTOR, *Collocation methods for nonlinear differential equations on low-rank manifolds*, Linear Algebra and its Applications, 705 (2025), pp. 143–184.
- [8] A. DEKTOR AND L. EINKEMMER, *Interpolatory dynamical low-rank approximation for the 3+3d Boltzmann-BGK equation*, arXiv preprint arXiv:2411.15990, (2024).
- [9] A. DEKTOR, A. RODGERS, AND D. VENTURI, *Rank-adaptive tensor methods for high-dimensional nonlinear PDEs*, Journal of Scientific Computing, 88 (2021), p. 36.
- [10] M. DING, J.-M. QIU, AND R. SHU, *Accuracy and stability analysis of the semi-lagrangian method for stiff hyperbolic relaxation systems and kinetic BGK model*, SIAM Multiscale Modeling & Simulation, 21 (2023), pp. 143–167.
- [11] L. EINKEMMER, *A low-rank algorithm for weakly compressible flow*, SIAM Journal on Scientific Computing, 41 (2019), pp. A2795–A2814.
- [12] L. EINKEMMER, J. HU, AND L. YING, *An efficient dynamical low-rank algorithm for the Boltzmann-BGK equation close to the compressible viscous flow regime*, SIAM Journal on Scientific Computing, 43 (2021), pp. B1057–B1080.
- [13] L. EINKEMMER, K. KORMANN, J. KUSCH, R. G. MCCLARREN, AND J.-M. QIU, *A review of low-rank methods for time-dependent kinetic simulations*, arXiv preprint arXiv:2412.05912, (2024).
- [14] L. EINKEMMER AND C. LUBICH, *A low-rank projector-splitting integrator for the Vlasov–Poisson equation*, SIAM Journal on Scientific Computing, 40 (2018), pp. B1330–B1360.
- [15] W. GUO, J. F. EMA, AND J.-M. QIU, *A Local Macroscopic Conservative (LoMaC) low rank tensor method with the discontinuous Galerkin method for the Vlasov dynamics*, Communications on Applied Mathematics and Computation, 6 (2024), pp. 550–575.

- [16] W. GUO AND J.-M. QIU, *A low rank tensor representation of linear transport and nonlinear Vlasov solutions and their associated flow maps*, Journal of Computational Physics, 458 (2022), p. 111089.
- [17] W. GUO AND J.-M. QIU, *A conservative low rank tensor method for the Vlasov dynamics*, SIAM Journal on Scientific Computing, 46 (2024), pp. A232–A263.
- [18] H. HAMMER, H. PARK, AND L. CHACÓN, *A multi-dimensional, moment-accelerated deterministic particle method for time-dependent, multi-frequency thermal radiative transfer problems*, Journal of Computational Physics, 386 (2019), pp. 653–674.
- [19] G. E. HAMMOND, A. J. VALOCCHI, AND P. C. LICHTNER, *Application of Jacobian-free Newton–Krylov with physics-based preconditioning to biogeochemical transport*, Advances in Water Resources, 28 (2005), pp. 359–376.
- [20] G.-S. JIANG AND C.-W. SHU, *Efficient implementation of weighted ENO schemes*, Journal of Computational Physics, 126 (1996), pp. 202–228.
- [21] C. A. KENNEDY AND M. H. CARPENTER, *Diagonally implicit Runge-Kutta methods for ordinary differential equations. a review*, tech. rep., NASA Langley Research Center, 2016.
- [22] D. A. KNOLL AND D. E. KEYES, *Jacobian-free Newton–Krylov methods: a survey of approaches and applications*, Journal of Computational Physics, 193 (2004), pp. 357–397.
- [23] D. A. KNOLL, V. MOUSSEAU, L. CHACÓN, AND J. REISNER, *Jacobian-free Newton–Krylov methods for the accurate time integration of stiff wave systems*, Journal of Scientific Computing, 25 (2005), pp. 213–230.
- [24] D. A. KNOLL, W. VANDERHEYDEN, V. MOUSSEAU, AND D. B. KOTHE, *On preconditioning Newton–Krylov methods in solidifying flow applications*, SIAM Journal on Scientific Computing, 23 (2001), pp. 381–397.
- [25] O. KOCH AND C. LUBICH, *Dynamical low-rank approximation*, SIAM Journal on Matrix Analysis and Applications, 29 (2007), pp. 434–454.
- [26] K. KORMANN, *A semi-Lagrangian Vlasov solver in tensor train format*, SIAM Journal on Scientific Computing, 37 (2015), pp. B613–B632.
- [27] L. LI, J. QIU, AND G. RUSSO, *A high-order semi-Lagrangian finite difference method for non-linear Vlasov and BGK models*, Communications on Applied Mathematics and Computation, 5 (2023), pp. 170–198.
- [28] J. C. MANDAL AND S. M. DESHPANDE, *Kinetic flux vector splitting for Euler equations*, Computers & Fluids, 23 (1994), pp. 447–478.
- [29] V. MOUSSEAU, D. KNOLL, AND W. RIDER, *Physics-based preconditioning and the Newton–Krylov method for non-equilibrium radiation diffusion*, Journal of computational physics, 160 (2000), pp. 743–765.
- [30] H. PARK, L. CHACÓN, A. MATSEKH, AND G. CHEN, *A multigroup moment-accelerated deterministic particle solver for 1-D time-dependent thermal radiative transfer problems*, Journal of Computational Physics, 388 (2019), pp. 416–438.

- [31] S. PIERACCINI AND G. PUPPO, *Implicit–explicit schemes for BGK kinetic equations*, Journal of Scientific Computing, 32 (2007), pp. 1–28.
- [32] J. REISNER, A. WYSZOGRODZKI, V. MOUSSEAU, AND D. KNOLL, *An efficient physics-based preconditioner for the fully implicit solution of small-scale thermally driven atmospheric flows*, Journal of Computational Physics, 189 (2003), pp. 30–44.
- [33] W. A. SANDS, W. GUO, J.-M. QIU, AND T. XIONG, *High-order adaptive rank integrators for multi-scale linear kinetic transport equations in the hierarchical Tucker format*, arXiv preprint arXiv:2406.19479, (2024).
- [34] T. SHI, D. HAYES, AND J.-M. QIU, *Distributed memory parallel adaptive tensor-train cross approximation*, arXiv preprint arXiv:2407.11290, (2024).
- [35] W. T. TAITANO, D. A. KNOLL, AND L. CHACÓN, *Charge-and-energy conserving moment-based accelerator for a multi-species Vlasov–Fokker–Planck–Ampère system, part II: Collisional aspects*, Journal of Computational Physics, 284 (2015), pp. 737–757.
- [36] W. T. TAITANO, D. A. KNOLL, L. CHACÓN, J. M. REISNER, AND A. K. PRINJA, *Moment-based acceleration for neutral gas kinetics with BGK collision operator*, Journal of Computational and Theoretical Transport, 43 (2014), pp. 83–108.
- [37] T. XIONG, J. JANG, F. LI, AND J.-M. QIU, *High order asymptotic preserving nodal discontinuous galerkin IMEX schemes for the BGK equation*, Journal of Computational Physics, 284 (2015), pp. 70–94.
- [38] K. XU, L. MARTINELLI, AND A. JAMESON, *Gas-kinetic finite volume methods, flux-vector splitting, and artificial diffusion*, Journal of Computational Physics, 120 (1995), pp. 48–65.
- [39] N. ZHENG, D. HAYES, A. CHRISTLIEB, AND J.-M. QIU, *A semi-Lagrangian adaptive-rank (SLAR) method for linear advection and nonlinear Vlasov-Poisson system*, Journal of Computational Physics, 532 (2025), p. 113970.